On the Maintenance and Initiation of the Intraseasonal Oscillation in the NCEP/NCAR Reanalysis and the GLA and UKMO AMIP Simulations

Kenneth R Sperber,[1] Julia M Slingo,[2] Peter M Inness,[3] and William K-M Lau[4]

[1]Program for Climate Model Diagnosis and Intercomparison
Lawrence Livermore National Laboratory
Livermore, CA 94551, USA

[2]Department of Meteorology
University of Reading
Reading, RG6 6AU, United Kingdom

[3]Hadley Centre for Climate Prediction and Research
United Kingdom Meteorological Office
Berkshire, RG12 2SY, United Kingdom

[4]Goddard Space Flight Center
NASA, Code 913
Greenbelt, MD 20771, USA

This paper was prepared for submission to *Climate Dynamics*

Corresponding Author:

Dr. Kenneth R Sperber
Program for Climate Model Diagnosis and Intercomparison
Lawrence Livermore National Laboratory
P.O. Box 808, L-264
Livermore, CA 94551 USA
Phone: (510) 422-7720
Fax: (510) 422-7675
E-mail: sperber@space.llnl.gov

Table of Contents

Abstract

In this study, satellite derived outgoing longwave radiation (OLR) and the reanalysis from the National Centers for Environmental Prediction/National Center for Atmospheric Research (NCEP/NCAR) are used as verification data in a study of intraseasonal variability in the Goddard Laboratory for Atmospheres (GLA) and the United Kingdom Meteorological Office (UKMO) atmospheric general circulation models. These models simulated the most realistic intraseasonal oscillations (IO) of the 15 Atmospheric Model Intercomparison Project models examined by Slingo et al. (1995, 1996). During the active phase of the intraseasonal oscillation, convection is observed to migrate from the Indian Ocean to the western/central Pacific Ocean, and into the South Pacific Convergence Zone (SPCZ). The simulated convection, particularly in the GLA model, is most realistic over the western/central Pacific Ocean and the SPCZ. In the reanalysis, the baroclinic structure of the IO is evident in the eddy-streamfunction, and eastward migration of the anticyclone/cyclone pairs occurs in conjunction with the eastward development of convection. Both the GLA and UKMO models exhibit a baroclinic structure on intraseasonal time scales. The GLA model is more realistic than the UKMO model at simulating the eastward migration of the anticyclone/cyclone pairs when the convection is active over the western/central Pacific. In the UKMO model, the main heating is located off the equator, which contributes to the irregular structures seen in this model on intraseasonal time scales.

The maintenance and initiation of the intraseasonal oscillation has also been investigated. Analysis of the latent heat flux indicates that evaporative wind feedback and frictional wave-CISK (conditional instability of the second-kind) are not the dominant mechanisms for promoting the eastward propagation of the intraseasonal oscillation since evaporation to the west of the convection dominants. In the GLA model, enhanced evaporation tends to develop in-place over the west Pacific warm pool, while in the UKMO simulation westward propagation of enhanced evaporation is evident. It is suggested that lack of an interactive ocean may be associated with the models systematic failure to simulate the eastward transition of convection from the Indian Ocean into the western Pacific Ocean since examination of observed sea surface temperature (SST) and its relationship to the active phase of the intraseasonal oscillation indicates that the intraseasonal oscillation may evolve as a coupled ocean-atmosphere mode. Above normal SST to the east of the convection may play a role in maintaining the eastward evolution of convection, while decreasing SSTs near the western portion of the convective envelope are associated with the cessation of convection.

Return to Table of Contents

1. INTRODUCTION

The Madden-Julian (Intraseasonal) Oscillation is a dominant mode of variability in the tropics (Madden and Julian 1971, 1972). It has long been recognized that it is manifested on a time scale of ~30-60 days

through large-scale circulation anomalies, which occur in conjunction with eastward evolving convective anomalies. These features are strongest and most coherent during the boreal winter/spring when the western Pacific warm pool is centered at or near the equator. The intraseasonal oscillation (IO) tends to move most slowly over the Eastern Hemisphere where the convective signature is most readily apparent. The current paradigm suggests that while convection is active, the propagation is slow because the IO behaves like a moist Kelvin wave. Once the convection subsides, usually in the vicinity of the dateline, the IO behaves much like a dry Kelvin wave which has a faster phase speed. The response to the convection is a forced Rossby wave which is characterized by upper-tropospheric cyclones (anticyclones) that lead (trail) the convection. These characteristics of the life cycle of intraseasonal oscillations have been described by many authors (e.g., Knutson and Weickmann 1987, Rui and Wang 1990, Matthews 1993, Hendon and Salby 1994). Given the dominance of this mode of variability, and the fact that suppressed convection tends to precede and follow the active phase of the oscillation, the IO is a useful tool for medium- and long-range weather forecasting in the tropics.

The IO also influences the extratropics. As the tropical convective heating makes it way into the western/central Pacific, teleconnections into the extratropics have been noted (Ferranti et al. 1990, Lau and Chang 1992, Higgins and Schubert 1995, Higgins and Mo 1996). Ferranti et al. (1990) demonstrated that the tropical intraseasonal oscillation projects on to the Pacific/North American and North Atlantic oscillation patterns. Their numerical experiments indicated that Northern Hemisphere forecast skill scores were improved when tropical heating due to strong intraseasonal oscillations was captured. Similar results were found by Lau and Chang (1992). Thus, the IO is also important for medium- and extended-range weather forecasts in the extratropics.

The signature of the IO has also been observed in the ocean. Sea surface temperature (SST) variations of ~0.5°K have been observed in conjunction with the passage of intraseasonal oscillations (Krishnamurti et al. 1988, Gutzler et al. 1994, Zhang and McPhaden 1995). Also, during the Tropical Ocean Global Atmosphere Coupled Ocean Atmosphere Response Experiment (TOGA-COARE), intraseasonal oscillations were observed to initiate downwelling oceanic Kelvin waves in the equatorial Pacific Ocean, which had the effect of shifting the warm pool slightly eastward (Weickmann et al. 1994). Thus, the IO is truly a global scale phenomenon, affecting both the atmosphere and ocean, and even the length of day via modulation of the Earth's angular momentum (Rosen and Salstein 1983). The IO merits much additional observational, modelling and theoretical investigation especially since theories regarding its initiation and maintenance are the subject of much debate (e.g., Hayashi and Golder 1993, Chao and Lin 1994).

The simulation of intraseasonal oscillations by general circulation models has been problematic. Models typically fail to capture the dominant periodicity of the intraseasonal oscillation, simulating oscillations that are usually weaker and not as spatially coherent as observed, and with the correct seasonality not well reproduced (Hayashi and Golder 1986, 1988, Lau and Lau 1986, Pitcher and Geisler 1987, von Storch et al. 1988, Park et al. 1990, and Slingo and Madden 1991). All of these shortcomings were manifested to one degree or another in the suite of 15 atmospheric general circulation models (GCMs) analyzed by Slingo et al. (1995, 1996). Their analysis used daily time-longitude output of 10°N-10°S averaged upper-tropospheric velocity potential and zonal wind from 10-year simulations of the period 1979-88. These simulations were performed as part of the Atmospheric Model Intercomparison Project (AMIP) in which the models were integrated using the same monthly mean SST data (Gates 1992, WMO 1995). The amplitude of 20-100 day bandpass filtered zonal mean u-wind was found to be useful for quantifying the ability of the models to simulate the IO. Based on this stratification, it was found that models with weak seasonal cycles underestimated the strength of the IO. Also, the models with the

strongest IO's were best at simulating the observed rainfall/SST relationship over the warm pool during northern winter. This may be important from the point of view of the current paradigm of the IO, which hypothesizes that it is a moist Kelvin wave maintained by diabatic heating. Models with weak convection over the warm pool would be less likely to maintain eastward propagation of the wave since it would dissipate more quickly due to insufficient heating. Additional results from that study also suggest that improved simulation of the climatology and the seasonal cycle by GCMs may result in better IO's. Stratification according to physical parameterization strongly suggested that the quality of the IO variability is linked to the type of closure used in the convective parameterization, with buoyancy closure being preferable to moisture convergence.

While the afore-mentioned difficulties are somewhat discouraging, the purpose of this paper is to evaluate the spatial and temporal evolution of intraseasonal oscillations in the Goddard Laboratory for Atmospheres (GLA) and the United Kingdom Meteorological Office (UKMO) GCMs, two of the models with the most realistic IO's from Slingo et al. (1995, 1996). These models were most realistic in that they simulated 20-100 day bandpass filtered 200hPa velocity potential and zonal wind anomalies of similar magnitude to the European Centre for Medium-Range Weather Forecasts /Joint Diagnostics Project (ECMWF/JDP) analyses. Even so, these models failed to reproduce the observed broad spectral peak in the 40-60 day interval based on the average power spectrum of all years of data. However, there were limited periods when these two models produced intraseasonal oscillations that were well defined, and with the correct periodicity. For such periods the life cycle of the IO will be studied through the analysis of streamfunction, outgoing longwave radiation (OLR), and other dynamical/physical quantities. In Section 2 the models and verification data are described, and in Section 3 the climatological base state is presented. In Section 4 the convective evolution and vertical structure of the IO is analyzed using EOF and correlation analysis, and in Section 5 various maintenance mechanisms are evaluated. The role of SST and the possibility that the IO is a coupled ocean-atmosphere mode is discussed in Section 6, and general discussion and conclusions are presented in Section 7.

Return to Table of Contents

2. THE MODELS AND DATA

The National Centers for Environmental Prediction/National Center for Atmospheric Research (NCEP/NCAR) reanalysis (Kalnay and Jenne 1991, Kalnay et al. 1996) and satellite derived OLR (Gruber and Winston 1978, Gruber and Krueger 1984) from the National Oceanic and Atmospheric Administration (NOAA) are the main data sets used for verification of the simulations. Subsequently, the NCEP/NCAR reanalysis is simply referred to as the reanalysis, while other analysis products are referred to explicitly ECMWF/JDP analysis, National Meteorological Center [NMC] analysis). The reanalysis data set is generated using a "frozen" state of the art data assimilation scheme and model. As such, this data set is based on a homogeneous system, and hence does not suffer from inconsistencies introduced by changing models and assimilation schemes which characterize the previous ECMWF/JDP and NMC analyses. Although the satellite derived OLR and reanalysis data is available for a longer record, we concentrate on 1979-88 (unless otherwise specifically mentioned) since this corresponds to the period over which the AMIP integrations were performed.

The GLA model analyzed here is version GCM 01.0 AMIP-1, circa 1992. It is a gridpoint model with 4° latitude x 5° longitude resolution and 17 sigma levels in the vertical. Of particular relevance to this study, the convective parametrization is a modified version of Arakawa and Schubert (1974), in which different

values of the "critical cloud work function" are prescribed for different cloud types, including a parameterization of evaporation of falling rain applied to both large-scale and convective precipitation (Sud and Walker 1992, 1993).

The UKMO UM-Climate 1, circa 1993, is also analyzed. This is a gridpoint model with 2.5° latitude x 3.75° longitude resolution and 19 vertical sigma levels. The convection scheme is a modified version of the Yanai et al. (1973) mass-flux scheme. Both updrafts and downdrafts are represented, and specific details of the buoyancy closure are described in Gregory and Rowntree (1990). Comprehensive details of the lineage, physics, and numerics of these models (and all of the AMIP models) may be found in Phillips (1994).

In some cases, the data analyzed are bandpass filtered using a 20-100 day Lanczos filter to isolate more clearly intraseasonal variations. This filter was used extensively in Slingo et al. (1995, 1996), where its response function is given. Henceforth, data processed with this filter are referred to as the "filtered" data.

Return to Table of Contents

3. CLIMATOLOGICAL STRUCTURES

a. OLR: Time-mean and Variability

The time-mean OLR during northern winter, when the IO is most active, is shown in Fig. 1 from NOAA satellite observations, and for the models for the period of the AMIP integrations. The models do a reasonable job of representing the basic structures of the OLR. They capture the locations of the high OLR associated with the subsidence of the subtropical highs. In the western Pacific, where the reservoir of SST >28°C is substantial, the models generate deep convection. However, there are several noticeable differences that are particularly relevant to this study. Both models erroneously simulate convective maxima over the central Indian Ocean, while failing to produce low OLR in the vicinity of the Maritime continent. In the case of the UKMO model, the convective maxima in the Indian Ocean is displaced near 10°S. Also, in both models the minimum values of OLR over the western Pacific Ocean are not as low as observed.

Figure 2 shows the standard deviation of the OLR (based on 9-year average of the variance during each four month boreal winter period). As demonstrated in previous studies (e.g., Slingo et al. 1992), regions of the lowest average OLR are typically coincident with the largest variations in OLR as seen for the observations. While this is the case for the GLA model, the UKMO model tends to exhibit the largest OLR variations along the periphery of the low OLR values in the time mean (Fig. 1) This is particularly apparent over the Indian Ocean and western Pacific where the largest variations are located poleward of the OLR minima. The models also exhibit larger variations than observed. This was also noted by Slingo et al. (1995, 1996) with regard to the amplitude of the zonal wind on seasonal and intraseasonal time scales.

In observations the dominant heating on intraseasonal time scales occurs in the vicinity of the eastern Indian Ocean and the Maritime continent. This is shown in Fig. 2 where >20%percent of the total variance of OLR is associated with intraseasonal time scales (30-70 days). During individual winters (e.g., 1987/88) intraseasonal time scales can account for upwards of 50-60% of the total variance in OLR over the eastern Indian Ocean. Substantial intraseasonal modulation of convection over Southeast Asia,

Australia and in the South Pacific Convergence Zone (SPCZ) is also observed. For the GLA model, the fraction of total variance explained by intraseasonal time scales is smaller and less coherent than observed. A local maxima is located over the central Indian Ocean coincident with the OLR minima seen in Fig. 1. Also, there is a pronounced underestimate of intraseasonal variability near Indonesia. This is also the case for the UKMO model, which simulates bimodal off-equatorial intraseasonal variability over the western Pacific Ocean.

b. Rotational Flow Response

In this section we describe the current paradigm of the intraseasonal oscillation using EOF analysis of filtered eddy-streamfunction and show the dominant rotational wind structures. For the reanalysis and models, the filtered data is generated on their respective longitude/latitude grids. Prior to the calculation of the EOF's, the data is area-weight interpolated to an 8° x 10° latitude/longitude grid. Cosine latitude weighting has been used in the calculation of the EOF's.

The current paradigm of the intraseasonal oscillation is that it is a Kelvin wave/Rossby wave interaction. The Kelvin wave signature of the intraseasonal oscillation is most readily identified in upper-tropospheric velocity potential (not shown). Time-longitude plots of upper tropospheric filtered ECMWF/JDP analyses (Hoskins et al. 1989) have been presented in Slingo et al. (1995, 1996). Space-time decomposition of this unfiltered data demonstrate the dominance of the eastward propagating wave-1 IO signature with a periodicity of ~50 days (not shown). The response of the rotational flow to the convective heating anomalies is a Rossby wave pattern (Knutson and Weickmann 1987, Rui and Wang 1990). Matthews (1993) showed this response pattern in an EOF analysis of ECMWF/JDP 150hPa eddy-streamfunction that was filtered to isolate intraseasonal time scales. This pattern is shown in Fig. 3 for DJF for the period 1982/83-1989/90. As indicated by the schematic diagram in Fig. 3, during the active phase of the IO, cyclones lead the heating anomalies associated with the increased planetary scale divergence over the Maritime continent, and an anticyclone pair trails. EOF analysis of the reanalysis data set for the same period demonstrates these same features with minor modification. The older ECMWF/JDP and NMC analyses were subject to uncertainties introduced by changing assimilation schemes and models. Even so, from ~1985 onward, the time-longitude filtered upper tropospheric velocity potential from the ECMWF/JDP analyses and the reanalysis are typically consistent in magnitude and phase. These results confirm the robustness of the dominant patterns of the rotational and divergent flow associated with the IO. In the remainder of the paper the reanalysis data set is used for verification.

During the AMIP decade, nine winter/spring periods (November-May 1979/80-1987/88) are available from which we generate the first two EOF's of the 200hPa eddy-streamfunction from the reanalysis, and the GLA and UKMO simulations (Fig. 4). As in Fig. 3, EOF-1 from the reanalysis is the forced Rossby wave response to the divergent outflow. EOF-2 corresponds to an eastward displacement of the trailing anticyclones. EOF-1 in conjunction with EOF-2 describe the eastward translation of the 200hPa eddy-streamfunction anticyclone/cyclone complex as the intraseasonal convective heating migrates to the east. EOF-1 from the GLA model is similar to that from the reanalysis, although the eddy-streamfunction complex is displaced to the west, being centered over the Indian Ocean near the OLR minima seen in Fig. 1. In EOF-2 an eastward displacement of the trailing anticyclones is seen, particularly in the Southern Hemisphere. As for the reanalysis, these two EOF's in combination represent the eastward propagation of the Rossby wave response. However, the GLA model simulates a more distinctive extratropical wave train pattern in the Northern Hemisphere than suggested by the reanalysis. For the

UKMO model, EOF-2 more closely represents EOF-1 from the reanalysis based on the location of the trailing anticyclones. The leading cyclones over the Maritime continent are weak, and an extratropical wave-train pattern dominates. EOF-1 is an eastward displacement of the trailing anticyclones akin to that observed from EOF-2 of the reanalysis. In the reanalysis, these IO related eddy-streamfunction loadings account for 23% of the variance of periods between 20 and 100 days. However, the percent variance explained by these modes is lower in the models than for the reanalysis, indicating that the simulated IO time scales are noisier. This is consistent with the results presented in Slingo et al. (1995, 1996).

Return to Table of Contents

4. INTRASEASONAL OSCILLATION CASE STUDIES

Many previous studies have used various techniques (regression, EOF analysis, etc.) to generate composite life cycles of the IO based on many years of data (e.g., Knutson and Weickmann 1987, Rui and Wang 1990, Hendon and Salby 1994). While using many years of data retains the large scale characteristics of the mode in question, it is desirable to analyze case studies in an effort to address specific (and perhaps localized) processes/mechanisms which may be operative and otherwise obscured from compositing over many years (e.g., Matthews et al. 1996). Also, more importantly from a modelling point of view, the GCMs exhibit difficulty at simulating coherent intraseasonal oscillations. Space-time spectra and time-longitude plots of 10°N-10°S averaged filtered 200hPa velocity potential presented in Slingo et al. (1995, 1996) indicated that no model was able to capture the dominance of the intraseasonal oscillation found in the ECMWF/JDP analyses. However, in the case of the GLA and UKMO models, when a clear eastward propagating signal is evident, the period of the oscillation is realistic. (The NCAR CCM2 AMIP model also showed similar realistic intraseasonal variations on occasion, but high frequency (daily) longitude-latitude data were not available with which to perform an analysis for this paper.) Therefore, in order to show the models in their best light, we examine the winter/spring period during which these models exhibited their strongest and most coherent intraseasonal oscillations. In the case of the GLA model, the winter of 1986/87 exhibited the best intraseasonal oscillations, while the winter 1980/81 from UKMO will be analyzed. These will be compared with the winter of 1987/88 from observations and the reanalysis.

1987/1988 was observed to be a period of particularly active intraseasonal variability (Matthews et al. 1996), which can be seen in the time-longitude plot of 10°N-10°S averaged filtered 200hPa velocity potential from the reanalysis (Fig. 5). Coherent eastward propagation is evident, with the intraseasonal oscillation making several apparent circuits of the globe from November through May with a period of ~45 days. As we are interested in the convection associated with the passage of the active phase of the IO in the vicinity of the Austral monsoon, and as noted earlier this is also the region where the heating associated with the intraseasonal oscillation tends to be strongest, we average the filtered velocity potential between 100°-140°E. The resulting pentad averaged IO index, also presented in Fig. 5, has been standardized by removal of the mean and dividing by the standard deviation (based on 17 years of reanalysis 1979-1995). As we can see, the amplitude of the intraseasonal oscillation exceeds +/-3 standard deviations during February and March 1988. This IO index, and those generated from the model case studies, are used in the correlation analyses presented throughout this paper in which we examine the relationship of the IO to convection, filtered streamfunction, filtered latent heat flux, and filtered SST.

a. Convective Evolution

In order to examine the convection associated with the intraseasonal oscillation, we correlate the observed IO index from Fig. 5 with pentad averaged NOAA OLR. It is important to note that the OLR data has not been filtered in an other way. In Fig. 6 the correlations of the IO index and OLR at various time lags are shown for the 1987/88 seven-month case study period. These panels show the spatio-temporal evolution of the convection associated with the intraseasonal oscillation. The convention is such that a negative IO index (the active phase of the intraseasonal oscillation) is associated with reduced OLR. Thus, positive correlations indicate enhanced convection. Enhanced convection (suppressed convection) significant at ≥95% confidence level is shaded grey (black). At day -15, a small region of enhanced convection is located over the tropical western Indian Ocean. Over the western Pacific Ocean a large region of suppressed convection is observed. At day -10 enhanced convection extends over most of the tropical Indian Ocean, and the suppressed convection is now dominant near the SPCZ. The development of convection over the eastern Indian Ocean is readily apparent by day -5. At a lag of 0 days, enhanced convection covers the eastern Indian Ocean and Maritime continent, from 10°N extending southward over Australia. The convection is most developed at this time in the vicinity of the region from which we generated the IO index (100°-140°E, 10°N-10°S, the box in the day -15 panel). At positive time lags, the convection associated with the intraseasonal oscillation is found further east. Enhanced convection near the SPCZ is noted at lags of +10 and +15 days as the convection weakens and diminishes in spatial extent. At this time suppressed convection develops over the Indian Ocean subsequent to passage of the active phase of the oscillation (day +10 and day +15). While the spatial extent of the convective envelope varies from year to year, it consistently exhibits the contiguous eastward transition from the Indian Ocean through to the western Pacific. Eastward development of convective anomalies over this region were noted by Kousky (1985) during the winter 1984/85 in a time-longitude plot of NOAA OLR. The spatio-temporal evolution of the intraseasonal convective anomalies in Fig. 6 is consistent with the one-point correlations of broadband OLR presented by Lau and Chan (1985), the development described in Weickmann et al. (1985), the convective life-cycle of the intraseasonal oscillation presented in Hendon and Salby (1994), and the extended EOF analysis of Lau and Chan (1985) and Murakami et al. (1986).

To represent concisely the spatio-temporal evolution of the enhanced convection seen in Fig. 6, we plot in Fig. 7 the time lag at which the positive correlation between the IO index and the OLR is a maximum. Data is plotted only at those gridpoints for which the correlation coefficient is significant at ≥95% confidence level. (At each gridpoint there are 7 correlation coefficients corresponding to the different lag correlations, as seen in Fig. 6. We then only consider positive correlations significant at ≥95% confidence level [shaded grey in Fig. 6], plotting in Fig. 7 the time lag at which the positive correlation is a maximum. This indicates the time when the convection is most enhanced with respect to the IO index). The associated maximum correlations are contoured over the time lags to provide information regarding the strength of the relationship. Results from the GLA and UKMO cases studies are also presented in Fig. 7.

Serial correlation may reduce the effective degrees of freedom used to estimate the 95% confidence level (currently 41 degrees of freedom are assumed based on correlating 43 pentads of data). However, the coherent spatial signature of the correlation coefficients and the lag structure seen in Fig. 6 and Fig. 7 indicate the IO index/OLR association is physically based. Also, while a more stringent estimate of the degrees of freedom would reduce the area of the convective signature, the associated eastward translation of the convection would remain intact.

Clearly, at negative time lags the observed convection is enhanced west of region from which we obtained our IO index. From day -15 through day -5 the convective envelope expands eastward into the eastern Indian Ocean. Both models fail to capture this eastward transition of enhanced convection over the Indian Ocean. This shortcoming also occurs in other years of the simulations, and is also seen in the seasonal variance statistics on IO time scales (Fig. 2). On day 0 through day +5 the observed convection is enhanced over the Maritime continent, extending southward over Australia. This is the time when the models first generate realistic IO related convection, although the spatial extent of the simulated convective envelopes are not as extensive as observed. At subsequent time lags, the observed convection extends further east and into the SPCZ. The GLA model is most realistic in this regard, while the correlations from the UKMO model are particularly weak and not well defined (even in the mean state [Fig. 1] OLR $\leq$210w m^{-2} in the SPCZ is not produced by this model).

The strength and extent of the SPCZ OLR anomalies is interpretable in terms of the mechanism proposed by Matthews et al. (1996) by which ascent is excited over this region. Their mechanism was developed based on diagnostic analysis of the strong IO that occurred during late March 1988, and through the use of an idealized model to ascertain cause and effect. They concluded that ascent over the SPCZ, and hence enhanced convection, could be excited in response to the incursion of high potential vorticity air from the southern extratropics on the eastern flank of the upper-tropospheric anticyclone that is established as the forced Rossby model response to convection over Indonesia. Their idealized modelling studies indicated that the strength of the SPCZ excitation was sensitive to the latitude of the heating over Indonesia. The weak SPCZ signature in the UKMO case study presented in Fig. 7 is consistent with the heating near Indonesia being mainly confined north of the equator.

While the eastward propagation of the convective signature in these models shows some improvement relative to previous studies (e.g., Lau and Lau 1986, Pitcher and Geisler 1987, von Storch et al. 1988, Park et al. 1990, Slingo and Madden 1991), our results indicate that the models fail to simulate the close association of the 200hPa velocity potential IO index and convection (primarily over the Indian Ocean) seen on the observations. Where eastward migration of the OLR signature is found in the models, the spatial extent of the convective envelope is more confined than observed. Dynamical phenomena associated with these shortcomings will be discussed shortly.

b. Vertical Structure of the Rotational Flow

In Section 3b we presented evidence that the models simulated a Rossby-wave pattern at 200hPa on intraseasonal time scales. However, the anticyclone/cyclone pairs tended to be displaced from the locations seen in the reanalysis. We now present a similar analysis for the case studies discussed in Section 4a, and also include an analysis at 850hPa to evaluate the vertical structure of the IO. Also, the principal component time series are presented to provide information on the phase variations of the Rossby gyres, and their relationship to the IO indices used for the OLR correlations (Fig. 7).

Note: For the reanalysis and the models, the streamfunction (and velocity potential) were calculated from the u- and v-wind components. For the GLA model, there were missing data where the 850hPa pressure surface was below the orography. This occurred principally over the Tibetan Plateau, Antarctica, a portion of Greenland, and a few gridpoints over the Rockies and Andes. Since the sigma surface data were not available for vertical extrapolation over these locations, missing values of the zonal wind were interpolated as a function of longitude along each latitude circle. The missing values of meridional wind were interpolated as a function of latitude at each longitude. Where missing data existed around a

complete latitude circle (Antarctica), data from the previous (more equatorward) latitude circle was used. In order to test the utility of this interpolation procedure, a similar missing data mask was applied to the u- and v-wind data from the reanalysis at 850hPa, and the interpolation procedure applied to the daily data. The streamfunction calculation, bandpass filtering etc. were then applied to this filled data set as usual, with the result that the EOF's/PC's and streamfunction lag correlations with the IO index (Sections 4b and 4c) were virtually identical to those from the raw reanalysis. Thus, we conclude that this filling procedure does not detrimentally affect the diagnostics presented at 850hPa for the GLA model.

The reanalyzed and simulated EOF's of the 200hPa and 850hPa filtered eddy-streamfunction for the case study periods are presented in Figs. 8-10. Even for this seven month period, the first EOF at 200hPa from the reanalysis (Fig. 8) shows a Rossby-wave pattern similar to that presented in Fig. 4 for all winters. This rotational flow complex is clearly associated with the IO since its principal component (PC-1, thick solid black line in Fig. 8) varies in-phase with the IO index (thick solid grey line) used for the OLR correlations in Section 4a. During the active phase of the intraseasonal oscillation (negative IO index) a leading cyclone pair, and a trailing anticyclone pair are centered about the upper-level outflow region in the vicinity of maximum heating near the Maritime continent. The second EOF is in quadrature with the first, with the anticyclone pair displaced to the east over the Maritime continent. The second PC at 200hPa, denoted by the thick dashed black line in Fig. 8, is out of phase with PC-1. Together these two EOF modes describe the migration of the rotational flow associated with the eastward propagation of the intraseasonal oscillation. That this was a year of very strong intraseasonal activity is reflected in the percent variance explained by these two EOF modes at 200hPa. In Fig.4 based on nine winter/springs, these two modes accounted for 23% of the filtered eddy-streamfunction variance, while for the period of this case study these modes explain 42% of the variance. Lau and Lau (1986) and Pitcher and Geisler (1987) found similar quadrature spatial displacements and temporal phases shifts of the first two EOF/PC's in upper-tropospheric velocity potential in GCM simulations. However, in both studies the period of the oscillation was 25-40 days.

As seen in Fig. 9 for the GLA case study, the first two filtered eddy-streamfunction EOF's at 200hPa are consistent with those presented in Fig. 4. As suggested by the westward displacement of EOF-1 at 200hPa relative to the reanalysis, PC-1 and a filtered velocity potential IO index centered over the Indian Ocean (60°-100°E, 10°N-10°S average, thin grey line) vary in-phase with each other. The IO index used for the OLR correlation in Fig. 7 (thick grey line) lags the Indian Ocean IO index by 5-10 days. Consistent with the reanalysis, PC-1 and PC-2 at 200hPa are (usually) out of phase with each other. These modes explain 37% of the IO time scale variance, significantly greater than noted for the nine winter/springs presented in Fig. 4 (18%), but less than that in the reanalysis case study, indicating that more simulated EOF's are needed to account for the same amount of observed variance.

For the UKMO case study (Fig. 10), the first 2 EOF's of 200hPa filtered eddy-streamfunction are similar to those from the GLA simulation over the tropical eastern hemisphere, with a westward displacement of the Rossby gyres in EOF-1. However, as in Fig. 4, the UKMO model EOF's are dominated by an extratropical wavetrain, unlike the reanalysis and the GLA simulation. Also, the phase relationships of the principal component time series, clearly defined in the reanalysis, are only present for limited periods (e.g. November and January/February).

To examine the vertical structure of the IO in the reanalysis, the first two EOF's and PC's of the rotational flow at 850hPa are also presented in Fig. 8. The first principal component at 850hPa (thin solid black

line) varies in phase with PC-1 at 200hPa. Thus, the loadings of the 850hPa EOF-1 denote leading anticyclones and trailing cyclones consistent with low-level convergence in the vicinity of maximum heating during the active phase of the IO. The second principal component at 850hPa (thin dashed black line in Fig. 8) varies in phase with PC-2 at 200hPa. Thus the first two modes are clearly baroclinic. It is noticed that the EOF's at 850hPa are displaced slightly east of those at 200hPa, thus indicating a westward vertical tilt. A westward tilt in the zonal wind was noticed by Murakami and Nakazawa (1984) and Park et al. (1990) in their analysis of observed intraseasonal variations. In addition, Park et al. (1990) demonstrated that the GLA (an earlier version) and GLAS (Goddard Laboratory for Atmospheric Sciences) models simulated a westward vertical tilt. Also, Slingo and Madden (1991) found a westward tilt, with precipitation leading upper-tropospheric velocity potential by 0.10 cycle for periods of 10- to 30-days in a perpetual January simulation with CCM1.

The GLA model also simulates the baroclinic structure in the rotational flow response (Fig. 9), but the presence of a westward vertical tilt is not well defined. The baroclinic structure is only clearly evident for a limited time period. From mid-January through May, PC-1 at 850hPa usually varies in-phase with PC-1 at 200hPa. The in-phase variation of PC-2 at 200hPa and 850hPa is more tenuous. Thus, baroclinicity of the IO simulated by this model is most evident in the first EOF. In the UKMO simulation, the baroclinic structure is evident in both EOF's, but only when the proper phase relationships of the principal components are reproduced. This relationship is less robust than that expressed by the GLA model, being most evident only during November and January/February. At 850hPa approximately the same amount of variance is explained as at 200hPa in the reanalysis and models respectively.

These results indicate that the vertical structure of the eddy-streamfunction is baroclinic on intraseasonal time scales, with the 200hPa and 850hPa out-of-phase eddy-streamfunction anomalies propagating to the east in near unison. The models capture these relationship less effectively. The baroclinic structure of the intraseasonal oscillation, initially noticed in the winds by Madden and Julian (1971, 1972), has also been noted by many other authors (e.g., Krishnamurti and Subrahmanyam 1982, Lau and Lau 1986, Knutson and Weickmann 1987, Gutzler and Madden 1989, Rui and Wang 1990, and Slingo and Madden 1991). The symmetry of the anticyclone/cyclone pairs about the equator is consistent with the composite life cycle presented in Rui and Wang (1990). The symmetry of the Rossby wave response, and the vertical tilt will be explored in more detail in the next subsection.

c. Spatio-Temporal Evolution of the Rotational Flow

In the same way that we used lag correlation analysis to show the spatio-temporal evolution of enhanced convection during the active phase of the IO (Fig. 7), we can clearly show the propagation of the filtered eddy-streamfunction during the active phase of the IO by correlation with the IO indices used in Section 4a. This is useful because it clearly demonstrates the translation of the Rossby wave streamfunction complex. Additionally, the correlation analysis provides information regarding the vertical tilt of the oscillation.

Given the sign convention that the active phase of the IO corresponds to a negative IO index, a positive correlation with the filtered eddy-streamfunction in the Northern Hemisphere corresponds to a cyclone. In the Southern Hemisphere, a positive correlation corresponds to an anticyclone. Conversely, a negative correlation in the Northern (Southern) Hemisphere is associated with an anticyclone (cyclone). To clearly portray the evolution of the bandpass filtered streamfunction anomalies, we have combined the lag

information of the positive (negative) correlations in the Northern Hemisphere with the negative (positive) correlations in the Southern Hemisphere to show the spatio-temporal evolution of the cyclone (anticyclone) pairs. As with the OLR, the lags are plotted where the confidence level of the correlation coefficient is ≥95%.

Note: in Fig. 11 we only plot lags for the strongest negative and positive correlations out to +/- 15 days in order to facilitate comparison with the OLR lags presented in Fig. 7. That the +15 day and -15 day lags are adjacent to each other does not imply that the period of the IO is 30 days. The actual maximum and minimum lag correlations near this boundary interface occur at longer lag and lead times, yielding an IO periodicity of ~45 days in the reanalysis case study. Extending the +/- lag window only serves to increase the spatial resolution of the eastward propagation in the vicinity of the +15 day and -15 day boundary.

Figure 11 shows the migration of the filtered eddy-streamfunction anomalies at 200hPa and 850hPa from the reanalysis and the models. Confining our attention to the subtropics, at 200hPa for zero time lag with respect to the IO index (yellow shading; recall the IO index is based on the region 100°-140°E, 10°N-10°S), we see that the leading cyclones are situated east of the date line ahead of the enhanced convection (Fig. 7). The trailing anticyclones are located over the western Indian Ocean to the west of the enhanced convection. At 850hPa the baroclinic nature of the rotational anomalies is evident, with an anticyclone (cyclone) pair leading (trailing) the enhanced convection as depicted in the schematic diagrams in Fig. 11. These locations are consistent with the EOF-1 patterns for 200hPa and 850hPa in Fig. 8. The GLA model readily simulates the location of the Rossby gyres at 200hPa and 850hPa for convection over the Maritime continent, while in the UKMO simulation the lag information is less coherent.

During the onset of convection in the western Indian Ocean (day -15), the trailing 200hPa (850hPa) anticyclones (cyclones) in the reanalysis are not well established, and the convection tends to be located west of the leading 200hPa (850hPa) cyclones (anticyclones). From day -10 through day +10, the enhanced convection over the Indian Ocean and the western Pacific tends to be situated at the interface of the cyclone/anticyclone pairs (as per the schematics in Fig. 11). However, once the convection approaches the dateline (day +15), it tends to be situated in-between the trailing 200hPa (850hPa) anticyclones (cyclones). At this time the leading 200hPa (850hPa) cyclones (anticyclones) are weaker and not well defined. In the GLA model, the western/central Indian Ocean convection on days -15 and -10 is principally associated with the leading anticyclones at 850hPa. (In the reanalysis this only occurs at day -15). The trailing cyclones at 850hPa do not begin to develop in the Eastern Hemisphere until day -5 when the convection first arises over the Maritime continent. This staggered development of the trailing cyclones is consistent with the failure of this model to simulate the clear eastward propagation of convection over the Indian Ocean found in the observed data, and is associated with the westward propagating OLR lag signature over the central/western Indian Ocean (Fig. 7) where convection over the Indian Ocean occurs at the juncture of the trailing cyclones. In the UKMO model the eastward migration of the filtered eddy-streamfunction complex is sporadic, and not as coherent as in the reanalysis and GLA simulation.

In the reanalysis the establishment of the trailing anticyclones at 200hPa when convection develops in the central Indian Ocean, and the location of the convection in-between the 200hPa trailing anticyclones when convection nears the dateline were also seen in the IO life-cycle study of Hendon and Salby (1994) using ECMWF and NMC analyses. Knutson and Weickmann (1987) identified a similar spatial

relationship between convective anomalies and 250hPa streamfunction using NMC analyses. However, they found the streamfunction pattern to be asymmetrical, with the Northern Hemisphere anomalies being "most prominent." Alternatively, Rui and Wang (1990) found the streamfunction anomalies to be more symmetrical about the equator, but stressed the association of the tropical convective anomalies with the trailing "upper- (lower-) anticyclonic (cyclonic) circulation anomalies." They also indicated that "the low-level circulation anomalies dissipate after the convection anomaly passes the western Pacific." However, the lags in Fig. 11 suggest that the 850hPa cyclones continue to propagate downstream in the reanalysis. Differences between the results presented here and those of Knutson and Weickmann (1987) and Rui and Wang (1990) are most likely due to our use of a single case study period rather than compositing over many years of data. Also, it is possible that the different characteristics are associated with the different prefiltering techniques applied to the dynamical fields. While we have filtered the eddy-streamfunction data, Rui and Wang (1990) retained higher frequency time scales through pentad averaging of data from which only the seasonal cycle was removed. Thus, higher frequency variations probably influenced their rotational signature, particularly when the IO related convection was weak. Also, the different data sets and analysis techniques may have contributed to the discrepancies noted above.

In both hemispheres, the eddy-streamfunction lags in Fig. 11 for the reanalysis are essentially symmetrical about the equator. The symmetrical nature of the rotational flow is also reflected in the magnitude of the correlations (not shown), typically being >|0.6| in the subtropics of each hemisphere when convection is active over the Eastern Hemisphere. The lags indicate that the spatial structure of this streamfunction complex remains fairly uniform as the convection migrates eastward from the Indian Ocean into the western Pacific. The GLA model has similar characteristics, but only when the convection is located over the western/central Pacific Ocean.

It is of interest to note that the 850hPa cyclone/anticyclone phase lags are displaced slightly to the east of their 200hPa anticyclone/cyclone counterparts in the reanalysis. This indicates that there is a westward vertical tilt to the eddy-streamfunction anomalies, with the low-level convergence leading the upper-level divergence. For the GLA model, the correlation analysis establishes the presence of the westward vertical tilt which was not evident in the EOF analysis.

The major shortcoming of the models is their poor performance over the Indian Ocean. Common features between the models and observations/analyses are most apparent when convection is active over the western/central Pacific. At such times, both models simulate eastward propagating convective anomalies and forced Rossby wave gyres which have a baroclinic structure on intraseasonal time scales. These properties are however better simulated by the GLA model, whereas the UKMO model is much noisier. The IO-related Rossby wave structures are particularly poor in the latter model, and this is probably associated with the tendency for the main center of convection to be located north of the equator.

Return to Table of Contents

5. MAINTENANCE OF THE INTRASEASONAL OSCILLATION

Numerous theories of intraseasonal variability are prevalent in the literature (e.g., see Hayashi and Golder 1993 for a review). In wave-CISK (conditional instability of the second kind), the eastward propagation of the convective envelope is maintained through the selective amplification of Kelvin waves (Lau and Peng 1987). Consistent with the observed vertical structure of the IO, this mechanism

indicates a westward vertical tilt with height should be present. However, a major difficulty with wave-CISK is that the preferred periodicity of the dominant waves is shorter than observed due to the preferred amplification of high frequency growth rates. In frictional wave-CISK (Hendon and Salby 1994, Salby et al. 1994), meridional convergence at the surface leads to amplification of the convective anomaly when it occurs in-phase with the convergence at 850hPa through the generation of eddy available potential energy (EAPE). The amplification stage occurs while the convection is located over the western/central Indian Ocean. At subsequent times the surface convergence shifts further eastward, nearly 40-50° longitude ahead of the convection, where it is no longer in-phase with the convergence above the boundary layer. This results in decreasing EAPE, and decay of the disturbance.

The evaporative wind feedback mechanism (also known as wind-induced surface heat exchange, WISHE), as proposed by Emanuel (1987) and Neelin et al. (1987), considers the role of evaporation in the maintenance and propagation of the IO, and it is not mutually exclusive of the wave-CISK mechanism. Enhancement of the low-level easterlies about the equator ahead of the convection is assumed to result in increased evaporative fluxes, which in turn maintains the eastward propagation of convection.

In order to evaluate these mechanisms of IO maintenance, we use a longitudinal translation scheme to composite OLR, filtered divergence, surface winds, and latent heat flux in a frame of reference with respect to the eastward propagation of the intraseasonal oscillation as it propagates through a given domain. Lau et al. (1988) and Park et al. (1990) used this method in their model verification studies. As with Lau et al. (1988) and Park et al. (1990), we use pentad averaged bandpass filtered upper-level velocity potential to define the eastward propagation of the intraseasonal oscillation. These time-longitude data sets were presented in Fig. 7 for the reanalysis and models. In this scheme we define a longitudinal translation to isolate the active phase of the intraseasonal oscillation. This translation is denoted T- (using the notation of Park et al. 1990). For an a priori selected longitude range the following steps are performed at each pentad:

1) We calculate the average of the 200hPa filtered velocity potential in our predefined longitude range. This average is used as a weighting factor when the translation is performed on the field of interest. Thus, periods of strong intraseasonal activity are emphasized.

2) If this average is negative, the longitude of the velocity potential minima in the predefined longitude range is mapped to the zero longitude of the translation reference grid T-.

This translation can be applied to any field of interest (F) resulting in F-. Since the models and reanalysis are most consistent over the western Pacific, we perform the translation for the region 105°E-180°W. We choose to perform the translation on total OLR, total surface wind, and filtered divergence to compare with the results of Hendon and Salby (1994), and comment further on their frictional wave-CISK hypothesis. Additionally, we translate the total latent heat flux to evaluate the role of evaporative wind feedback, and to evaluate model performance.

a. OLR and Filtered Divergence

In this section translations are applied to OLR and filtered divergence (Fig. 12). There are two reasons for this: (1) use of total OLR to show more precisely the location, magnitude and spatial extent of deep convection about the wave center; (2) divergence is a very noisy field. For the UKMO simulation surface data were unavailable.

As Fig. 12 shows, the observed convection is slightly displaced to the west of the wave center. The OLR signature extends to 15°S along the eastern flank which is consistent with the convection observed in the SPCZ (Fig. 7). The baroclinic structure of the divergence at 850hPa and 200hPa, and the ambiguous signal at the surface are consistent with the results of Hendon and Salby (1994). In the GLA model the convection is more intense than observed as indicated by the lower values of OLR. The convection is located at the wave center, and it is more longitudinally confined than observed. This model does simulate a southeastward extension of convection which is associated with the SPCZ. The convection in the GLA model is more realistic than that of the UKMO model.

The presence of surface convergence (negative divergence) to the east of the convection in the reanalysis, and to some extent in the GLA simulation, indicates that an element of frictional wave-CISK is present. However, the importance of this convergence relative to that which is coincident with the convection has yet to be determined. In the GLA model, convergence at the surface is dominant in the vicinity of the convection, suggesting that convection is more closely tied to local boundary layer processes than suggested by the reanalysis. In the UKMO integration the more irregular structure in the divergence field is consistent with the weaker convective signature, and agrees with the split tropical convergence zones seen in Figs. 2 and 7 on intraseasonal time scales.

b. Latent Heat Flux, Surface Winds, and OLR

In Fig. 13, translations of the latent heat flux, surface winds (850hPa for UKMO) and OLR are presented. The most immediate result is that strong latent heat flux occurs coincident with, and to the west of the convection in the reanalysis and GLA simulation, where the surface winds exceed 4m s^{-1}. The tendency of the latent heat flux to be proportional to the windspeed is consistent with the TOGA-COARE in situ measurements presented by Zhang and McPhaden (1995) and Lau and Sui (1996). To the east of the convection, the latent heat flux is substantially lower (and less than the climatological mean, not shown) in the reanalysis. This result indicates that evaporative wind feedback (WISHE) is not the dominant mechanism for maintaining eastward propagation of the intraseasonal oscillation. This conclusion is consistent with the finding of Lau and Sui (1996) which was based on an analysis of surface fluxes from the Improved Meteorological Surface Mooring within the Intensive Flux Array (IFA) during the TOGA-COARE Intensive Observation Period (IOP).

In the GLA simulation the latent heat flux to the east of the convection does not exhibit as systematic a reduction, and in the UKMO simulation the strongest latent heat flux tends to occur coincident with the convection. Outside of the deep-tropics to the east of the convection in the reanalysis, the latent heat flux is larger where the meridional wind component is strong. This implies that characteristics of frictional wave-CISK are at work. In the GLA model the correspondence between the meridional wind and evaporation is strongest in the Northern Hemisphere, while in the UKMO model the flow is more zonal than indicated by the reanalysis.

The degree to which frictional wave-CISK is operative is an open question. Hendon and Salby (1994) went on to examine the behavior at 1000hPa, finding an eastward displacement of 40-50° in the location of convergence relative to that at 850hPa. This shift was ascribed to friction, and formed the basis for their frictional wave-CISK hypothesis. We looked for such a displacement of the surface (10m) winds from the reanalysis (since that is what is available from the model archive), and did not find evidence of such a displacement. The reanalysis surface filtered eddy-streamfunction lags (not shown) were

consistent with those at 850hPa (Fig. 11), and EOF analysis as in Fig. 8 (not shown) also indicated the surface and 850hPa to be in-phase with each other. This suggests that frictional wave-CISK may not be a dominant mechanism for maintenance of the IO. However, important questions that remain to be addressed with regard to this mechanism include: (1) How much does the large-scale atmospheric moisture convergence to the east of the convection contribute to the net moisture supply? (2) Is it substantial enough to override the below normal latent heat flux in this region? Answers to these questions are beyond the scope of the present paper, but further evidence of the regionality of the latent heat flux for the case study periods is explored using lagged correlation analysis in the next subsection.

c. IO Index/Filtered Latent Heat Flux Correlations

Filtered latent heat flux correlations with the IO index from reanalysis and the models are shown in Fig. 14. Negative correlations correspond to enhanced latent heat flux (evaporation). In the reanalysis, on day -15, convection is located near 60°E, 5°S (Figs. 6,7, and 15). To the west, near the Somali coast, a small region of enhanced latent heat flux is found, but its magnitude and spatial extent is quite small. However, enhanced latent heat flux is noticed extending ~30° to the southeast of the convection. This suggests that frictional wave-CISK may be important during initiation of IO related convection. However, it is conceivable that this enhanced latent heat flux is a symptom of the development of the leading anticyclones at 850hPa on day -15, the purple shading seen in Fig. 11, which occur as a consequence of the convection. In this latter scenario, the initiation of convection in the western Indian Ocean would be associated with local processes. However, from day -5 through day +15, enhanced latent heat flux at and to the west of the convection dominates. To the east of the convection, the positive correlations indicate that below normal evaporation extends well into the subtropics. This suggests that large-scale moisture convergence from east of the convection may not be dominant. The mechanism by which the IO propagates to the east is not as yet understood, and a possible scenario by which this occurs will be discussed in Section 6.

The lagged correlations for the GLA model (Fig. 14) provide a valuable qualification to the Lagrangian translation of the latent heat flux given in Fig. 13. The correlations clearly show that the enhanced evaporation develops in-place over the warm pool beginning when the convection first develops there on day -5. The dominant evaporation tends to remain over the warm pool, even on day +15 when convection is located near the dateline, thus giving the appearance that enhanced evaporation occurs to the west of the convection in the Lagrangian translation. This model appears to be more closely tied to local behavior over the warm pool than the variations from the reanalysis that occur over most of the eastern hemisphere as the IO develops and matures.

In the UKMO model, the main center of evaporation lies to the east of the convective signal on day -5 and day 0, when convection first becomes apparent over the Maritime continent (Fig.7). This suggests a WISHE type mechanism during onset in this model. Subsequently, when convection is near the dateline, evaporation from the west dominates which is more consistent with the reanalysis. This is an important difference relative to the GLA simulation and the reanalysis, namely that the UKMO evaporation tends to migrate to the west, whereas the GLA evaporation develops in place, while in the reanalysis the evaporation migrates to the east behind the convection.

The Lagrangian translation and correlation analysis indicate the importance of the latent heat flux at and to the west of the convection. These results confirm the in situ observations over the IFA during the TOGA-COARE IOP (Lau and Sui 1996), and indicate that these interactions are operative over the

oceans of the eastern hemisphere during the active phase of the IO. For the case study periods analyzed, the models do not simulate in a robust manner the enhancement of evaporation to the west to the convection. Thus, the physical mechanism by which the convection is maintained in the reanalysis is not well reproduced by these models. Since the reanalysis indicates that WISHE and frictional wave-CISK are not the dominant mechanisms by which the eastward propagation and time scale of the IO are established, other mechanisms of IO variability must be investigated.

Return to Table of Contents

6. THE INTRASEASONAL OSCILLATION: A COUPLED MODE?

The overall poor simulation of intraseasonal oscillations in the AMIP simulations is disturbing and perhaps suggestive that a fundamental process is lacking in AGCMs (Slingo et al. 1995, 1996). One such process may be the response of the SST to changes in the surface winds and fluxes associated with the IO. Krishnamurti et al. (1988) showed that anomalous fluxes associated with the IO may affect the SSTs in the West Pacific, and recent results from TOGA-COARE have suggested that SSTs are modulated coherently by the IO (e.g. Gutzler et al. 1994; Chen et al. 1996, Lau and Sui 1996, Zhang 1996a). Using weekly observed SST distributions, covering a number of years, Hendon and Glick (1996) showed that intraseasonal variations in SST (with root-mean-squared amplitude of ~0.5°K) are relatively important for the Indian and west Pacific Oceans when compared with the seasonal and interannual variability. Evidence of a coherent relationship between SSTs and atmospheric forcing at intraseasonal time scales has also been provided by Zhang (1996b) using an extended time series covering several years from the TOGA TAO (tropical atmosphere ocean) array. He notes that the intraseasonal variability of SST, although generally weaker than the seasonal and interannual variability, is easily detectable. He also notes that the coherence between the atmospheric forcing and the SST variations is significant for timescales in excess of 4-5 days, and that the atmosphere appears to force the SST.

Using a time-longitude cross-section of SST, and plotting its relation to OLR, Gutzler et al. (1994) suggested a relationship between SSTs in the Indian Ocean and the phase of the IO. They found that just prior to the onset of convection in the Indian Ocean, positive SST anomalies of ~0.5°K developed near 90°E, and subsequently the "positive SST anomalies appear to shift eastward ahead of the enhanced convection associated with the OLR anomalies." Flatau and Flatau (1996) have developed a conceptual model which suggests that modification of the SST by the convective system favors the development of positive SST anomalies ahead of the convection, and negative SST anomalies at and to the west of the convection that result in conditions favorable for the eastward migration of the convective envelope. Lau and Sui (1996) found SST warming over the IFA was associated with above normal shortwave radiation at the surface and below normal latent heat flux when IO related convection was located to the west. Subsequently, when convection was located east of the IFA, SST cooling was dominated by enhanced latent heat flux. This scenario is consistent with the west Pacific observations of Zhang (1996a), and suggests that the IO may be a coupled phenomenon which requires an interactive ocean surface to produce the correct organization of convection and its eastwards propagation. Investigation of the response by the atmosphere to such changes in SST requires further attention, particularly over the Indian Ocean.

In order to investigate the relationship between the IO and SST in more detail, we have correlated the IO index with filtered observed SST (and skin temperature over land) for the 1987/88 case study. The SST data is that which was used in the ECMWF (and NCEP/NCAR) reanalyses, and the skin temperature is

that produced from the ECMWF reanalysis (it was more convenient for us to gain access to the observed SST via the ECMWF reanalysis). In Fig. 15, these correlations are plotted as gridpoint data, while correlations of the IO index with OLR are plotted as isolines (same data as used in Fig. 6) in order to show the association between the SST and convection. As seen in Fig. 15, on day -15, the enhanced convection (blue contours) develops over a region of warm SST anomalies in the western Indian Ocean just south of the equator, and in the central Indian Ocean just north of the equator. Enhanced warming is also found along the equator extending to 90°E, which at day -10 is where the enhanced convection is strongest. At day -10 significantly warmer SST spreads south of the Indonesian peninsula near 115°E, 15°S, which is precisely where suppressed convective activity (and presumably enhanced subsidence) occurred during the previous pentad (day -15). Similarly, at day -5 the convection extends eastward to New Guinea and adjacent to northwest Australia, where above normal SST and suppressed convection were found on day -10. This cycle continues on day 0 where convection north of New Guinea is manifested. On day +5 through day +15 convection is found near 170°E, 5-20°S where warm SST anomalies developed previously, subsequent to suppressed convection.

In the vicinity of the enhanced convection, cloud shielding and enhanced latent heat flux serve to cool the local SST, resulting in a zonal gradient of SST with warmer values to the east that may provide the impetus for convection to develop further east. To the west of the convection evaporative cooling dominates, particularly over the Indian Ocean from day 0 through day +10 where below normal SST coincides with the enhanced latent heat flux seen in Fig. 14. As a result the western limit of the convection is eroded. This cycle of suppressed convection east of the convection, leading to increased SSTs and eastward migration of the convective envelope at subsequent pentads, with conditions in the west that serve to decrease SSTs and convection, is consistent with the Flatau and Flatau (1996) air-sea convective intraseasonal interaction (ASCII) mechanism for maintaining eastward propagation of the intraseasonal oscillation and observations over the western Pacific (Lau and Sui 1996, Zhang 1996a). Furthermore, our results suggest that it is the local gradient of SST that is important for the eastward migration. For example, as indicated in Fig. 15, the convection enhances eastward from the Indian Ocean into the western Pacific from day -10 through day 0, while the convection over the Indian Ocean remains intact on day -10 and day -5. Only on day 0 does the convection over the Indian Ocean begin to subside as cold SST anomalies develop where the evaporative cooling intensifies (Fig. 14). Thus, it appears the local SST gradient near the eastern boundary of the convective envelope is associated with the downstream development of convection, while the SST gradient near the western boundary is related to the cessation of convection.

It is likely that the warm SST anomalies to the east of the convection result as a consequence of upper-level outflow and subsidence. Such conditions would enable a shallow mixed surface layer to heat up via shortwave radiation in the presence of light winds. As shown previously in Fig. 13, the surface winds to the east of the convection are very weak during the active phase of the IO, thus evaporative cooling is not dominant at this local. However, near the western portion of the convective envelope the strength of the surface westerlies is such that evaporative cooling plays a dominant role in modulating the surface energy budget. This results in the cooling that is observed systematically behind the convection. The data suggest that the warm SST anomalies may be particularly important in the Indian Ocean. They may be associated with the onset of convection in the western Indian Ocean, and they appear to the lead the convection through to the western Pacific Ocean.

Over land, the surface skin temperature from the ECWMF reanalysis indicates that systematic cooling

and heating occur over the continental interior. The signal is actually first manifested in the observed SST in the vicinity of the Benguela current. The suppressed convection over the Atlantic Ocean on day -10 through day 0 (red contours) suggests enhanced subsidence, which in turn implies an intensification of the subtropical anticyclone. This in turn should result in enhanced coastal upwelling, which appears to be manifested as below normal SSTs that propagate northward along the west coast of Africa. Statistically significant below normal temperature anomalies are subsequently found over continental Africa, which may exceed 2-3°K during individual intraseasonal episodes. Conversely, on day +5 through day +15, above normal SSTs develop over the southeastern Atlantic Ocean and continental Africa which is consistent with lower OLR near the anticyclone. The lower OLR implies the presence of decreased subsidence, a weaker anticyclone, less coastal upwelling and warmer SST adjacent to the west coast of Africa. Convection is found over tropical Africa after the warming is established over the continent as the active phase of the IO establishes itself over the Eastern Hemisphere. Analysis of other case study periods would be beneficial in determining the robustness of these large-scale temperature fluctuations.

The results of the IO index/SST correlations indicate that large-scale surface temperature anomalies propagate to the east in conjunction with the passage of intraseasonal oscillations. The large-scale structure of this temperature signal might be useful for medium-range weather forecasting, particularly over land. However, the role the SST plays with regard to the initiation and eastward migration of IO-related convection can only be conclusively determined by using coupled ocean-atmosphere models.

Return to Table of Contents

7. DISCUSSION AND CONCLUSIONS

The NCEP/NCAR reanalysis data set is used in a study of observed and simulated intraseasonal variability. EOF analysis indicates that the large-scale structure of the IO-related rotational flow is consistent with the previous ECMWF/JDP and NMC analyses. Most encouraging is the regionally consistent relationship of the reanalysis and satellite derived OLR which clearly characterize the spatio-temporal evolution of the convectively driven forced Rossby wave response on intraseasonal time scales. The models perform best when the IO-related convection is over the Maritime continent. At such times the forced Rossby wave gyres are most well defined. The GLA model better simulates the eastward propagation of the convection and streamfunction anomalies over the western/central Pacific Ocean. In the UKMO simulation this signature is more irregular. A major shortcoming of both models is their inability to properly simulate the convection over the Indian Ocean, and its progression to the Maritime continent. Such eastward propagation over the oceans of the Eastern Hemisphere is a fundamental property of the IO that always occurs during the active phase of the oscillation in the correlation statistics. Thus, determining causes for the models failure to capture this signal is of fundamental importance.

Intraseasonal variability in an earlier version of the GLA model has previously been documented by Park et al. (1990). The results presented here indicate that the simulation of the IO has improved as this model has undergone development. The modifications to this models formulation have been numerous (Sud and Walker 1992, 1993), and therefore direct attribution to a specific modification which resulted in the improved IO simulation is not possible. However, it is believed that modification to the Arakawa-Schubert convection scheme, by including a minimum entrainment parameter and different "critical cloud work functions" and a more realistic parameterization of the physics of falling rain are the

primary sources of improved IO simulation. This belief is supported by the study of Tokioka et al. (1988) in which inclusion of an entrainment parameter in an Arakawa-Schubert convection scheme improved low-frequency eastward propagating waves in a GCM experiment. Other modifications that may have contributed to the IO improvement include a more sophisticated planetary boundary layer treatment, and increased vertical resolution.

While it is encouraging that documented improvement of intraseasonal oscillations in GCM's has occurred in recent years, there are still many problems to overcome. We have shown the GLA and UKMO models in their best light by selecting the periods when their intraseasonal oscillations were strongest and most coherent. During other years, simulation of the spatio-temporal evolution of the dynamical and convective signatures tend to be less coherent.

A factor to consider is the different horizontal resolutions that these two models have employed since simulation of the intraseasonal oscillation has been shown to be sensitive to this characteristic. In instances when a specific model has been run at a variety of horizontal resolutions, demonstrably poorer intraseasonal oscillations have been simulated as horizontal resolution was increased (Slingo et al. 1995, 1996; Gualdi et al. 1995). These authors found that deterioration of IO simulation was most significant when resolution increased from approximately T21 to T42. The GLA (4° latitude x 5° longitude) and UKMO (2.5° latitude x 3.75° longitude) models straddle these horizontal resolution regimes, and perhaps coincidently, the UKMO model simulated a more irregular intraseasonal oscillation than the GLA model. It may therefore prove a challenge for the GLA model to simulate coherent intraseasonal oscillations using increased horizontal resolution. Alternatively, the IO in a lower resolution version of the UKMO model may become more coherent. This is not meant to suggest that low resolution is preferable, but rather this conundrum symbolizes unknown shortcomings in our understanding of processes and scale interactions that occur at high resolution. The apparent decrease in skill at high horizontal resolution may be related to the closure of that convection scheme and its interaction with resolution. At approximately T42, tropical synoptic scale disturbances begin to be realized. Thus, it is possible that classes of higher frequency synoptic scale phenomena (e.g., cloud clusters, super-cloud clusters, westerly wind bursts etc.) are not properly represented. Thus, poorly simulated fast modes of variability may detrimentally affect slower modes. Proper simulation of such high frequency multi-scale phenomena may be crucial for simulating realistic intraseasonal variability (Chao and Lin 1994).

Analysis of the reanalyzed latent heat flux suggests that evaporative wind feedback (WISHE) and frictional wave-CISK are not the dominant mechanisms which promote the eastward migration of the IO during the case study period analyzed. Also, investigation of the relationship between the latent heat flux and observed SST indicates that warming of the SST in advance of the convection is a viable mechanism for promoting eastward migration of the convective envelope on intraseasonal time scales. Evaporative cooling is of minimal importance for the surface energy balance ahead of the convection. Thus, SSTs in this region warm, probably due to shortwave heating, thereby promoting eastward migration of the convection through a change in the local SST gradient. Conversely, evaporative cooling (and possibly cloud shielding) near the western portion of the convection is associated with decreasing SST and the cessation of convection. The monthly mean SSTs used for the AMIP integrations do not capture these regionally specific evolving anomalies. However, the use of weekly or daily observed SSTs as a boundary condition would not be the ideal solution for improved IO simulation since the synoptic state of a simulation would not be expected to agree with the observed synoptic state under which the SSTs were manifested. Additionally, the evidence presented suggests that the IO is a coupled air-sea mode. Thus, investigation of the IO using coupled ocean-atmosphere models is of paramount interest.

Although Slingo et al. (1995, 1996) discuss reasons for the poor simulation of IO variability, the overall lack of skill exhibited by the models suggests that the IO may have to be treated as a coupled mode. Thus, much fundamental research needs to be pursued both observationally, and in the modelling community. It is anticipated that additional insight will be gained from further analysis of data from the TOGA-COARE IOP during which several strong intraseasonal oscillations occurred. However, the dearth of in situ observations over the Indian Ocean is particularly troubling, especially given the models shortcomings over this domain. Extending the TOGA-TAO array into the Indian Ocean would be beneficial for understanding the ocean-atmosphere interactions over this region, and for the study of transitions between the Indian Ocean and western Pacific.

Return to Table of Contents

Acknowledgments

Special thanks to the NCEP/NCAR for making the reanalysis data set available, and the ECMWF for making the observed SST and reanalyzed skin temperature data available. We thank Dr. Jim Boyle (PCMDI/LLNL) for useful discussions, Dr. Harry Hendon (University of Colorado) for providing the observed OLR data, Dr. Mike Fiorino (PCMDI/LLNL) for facilitating access to the NCEP/NCAR reanalysis, Dr. Mike Pedder (University of Reading) for supplying the code for the computation of the filter weights, and Dr. Adrian Matthews (University of Reading) for providing the ECMWF/JDP 150hPa eddy-streamfunction EOF panel in Fig. 3. This work was performed under the auspices of the U.S. Department of Energy Environmental Sciences Division at the Lawrence Livermore National Laboratory under contract W-7405-ENG-48.

REFERENCES

Arakawa A, Schubert WH (1974) Interaction of a cumulus cloud ensemble with the large-scale environment, part 1. J Atmos Sci 31: 674-701

Chao WC, Lin S-J (1994) Tropical intraseasonal oscillation, super cloud clusters, and cumulus convection schemes. J Atmos Sci 51: 1282-1297

Chen SS, Houze RA Mapes BE (1996) Multiscale variability of deep convection in relation to large-scale circulation in TOGA COARE. J Atmos Sci (in press)

Emanuel, KA (1987) An air-sea interaction model of intraseasonal oscillations in the tropics. J Atmos Sci 44: 2324-2340

Ferranti L, Palmer TN, Molteni F, Klinker E (1990) Tropical-extratropical interaction associated with the 30-60 day oscillation and its impact on medium and extended range prediction. J Atmos Sci 47:2177-2199

Flatau M, Flatau PJ (1996) The role of SST feedback in the development of equatorial convection. Proceedings of the AMS Conference on the Global Ocean-Atmosphere-Land System (GOALS), Atlanta, Georgia, J124-J127

Gates WL (1992) AMIP: The atmospheric model intercomparison project. Bull Amer Meteorol Soc 73: 1962-1970

Gregory D, Rowntree PRR (1990) A mass flux convection scheme with representation of cloud ensemble

characteristics and stability dependent closure. Mon Wea Rev 118: 1483-1506

Gruber A, Winston JS (1978) Earth-atmosphere radiative heating based on NOAA scanning radiometer measurements. Bull Amer Meteor Soc 59: 1570-1573

Gruber A, Krueger AF (1984) The status of the NOAA outgoing longwave radiation data set. Bull Amer Meteor Soc 65: 958-962

Gualdi S, von Storch H, Navarra A (1995) Tropical intraseasonal oscillation appearing in operational analyses and in a family of general circulation models. MPI Report 165. Max Planck Institute for Meteorology, Bundesstrasse 55, D-20146, Hamburg, Germany J Atmos Sci (submitted)

Gutzler DS, Madden RA (1989) Seasonal variations in the spatial structure of intraseasonal tropical wind fluctuations. J Atmos Sci 46:641-660

Gutzler DS, Kiladis GN, Meehl GA, Weickmann KM, Wheeler M (1994) The global climate of December 1992-February 1993. Part II: large-scale variability across the tropical western Pacific during TOGA COARE. J Clim 7: 1606-1622

Hayashi YY, Golder DG (1986) Tropical intraseasonal oscillations appearing in a GFDL general circulation model and FGGE data. Part I: phase propagation. J Atmos Sci 43: 3058-3067

Hayashi YY, Golder DG (1988) Tropical intraseasonal oscillations appearing in a GFDL general circulation model and FGGE data. Part II: structure. J Atmos Sci 45: 3017-3033

Hayashi Y, Golder DG (1993) Tropical 40-50- and 25-30-day oscillations appearing in realistic and idealized climate models and the ECMWF dataset. J Atmos Sci 50: 464-494

Hendon HH, Glick J (1996) Intraseasonal air-sea interaction in the tropical Indian and Pacific Oceans. J Atmos Sci (submitted)

Hendon HH, Salby ML (1994) The life cycle of the Madden-Julian oscillation. J Atmos Sci 51: 2225-2237

Higgins RW, Schubert SD (1995) Simulations of persistent North Pacific circulation anomalies and interhemispheric teleconnections. J Atmos Sci 53:188-207

Higgins RW, Mo KC (1996) Persistent North Pacific circulation anomalies and the tropical intraseasonal oscillation. J Clim (submitted)

Hoskins BJ, Hsu HH, James IN, Masutani M, Sardeshmukh PD, White GH (1989) Diagnostics of the global atmospheric circulation based on ECMWF analyses 1979-1989. WCRP-27, World Meteorological Organization, Geneva.

Kalnay E, Jenne R (1991) Summary of the NMC/NCAR reanalysis workshop of April 1991. Bull Amer Meteor Soc 72: 1897-1904

Kalnay E, Kanamitsu M, Kistler R, Collins W, Deaven D, Gandin L, Iredell M, Saha S, White G, Woollen J, Zhu Y, Chelliah M, Ebisuzaki W, Higgins W, Janowiak J, Mo KC, Ropelewski C, Wang J, Leetmaa A, Reynolds R, Jenne R, Joseph D (1996) The NCEP/NCAR 40-year reanalysis project. Bull Amer Meteorol Soc 77: 437-471

Kousky VE (1985) The global climate for December 1984-February 1985: a case of strong intraseasonal oscillations. Mon Wea Rev 113:2158-2172

Knutson TR, Weickmann KM (1987) 30-60 day atmospheric oscillations: composite life cycles of convection and circulation anomalies. Mon Wea Rev 115: 1407-1436

Krishnamurti TN, Subrahmanyam D (1982) The 30-50 day mode at 850mb during MONEX. J Atmos Sci 39:2088-2095

Krishnamurti TN, Oosterhof DK, Mehta AV (1988) Air-sea interaction on the time scale of 30 to 50 days. J Atmos Sci 45: 1304-1322

Lau KM, Chan PH (1985) Aspects of the 40-50 day oscillation during the northern winter as inferred from outgoing longwave radiation. Mon Wea Rev 113:1889-1909

Lau KM, Chang, FC (1992) Tropical intraseasonal oscillation and its prediction by the NMC operational model. J Clim 5: 1365-1378

Lau KM, Peng L (1987) Origin of low frequency (intraseasonal) oscillations in the tropical atmosphere. Part I: basic theory. J Atmos Sci 44: 950-972

Lau KM, Sui CH (1996) Mechanisms of short-term sea surface temperature regulation: observations during TOGA-COARE. J Clim (in press)

Lau N-C, Lau WK-M (1986) The structure and propagation of intraseasonal oscillations appearing in a GFDL general circulation model. J Atmos Sci 43: 2023-2047

Lau N-C, Held IM, Neelin JD (1988) The Madden-Julian oscillation in an idealized general circulation model. J Atmos Sci 45: 3810-3832

Madden RA, Julian PR (1971) Detection of a 40-50 day oscillation in the zonal wind in the tropical Pacific. J Atmos Sci 28: 702-708

Madden RA, Julian PR (1972) Description of global-scale circulation cells in the tropics with a 40-50 day period. J Atmos Sci 29: 1109-1123

Matthews AJ (1993) The intraseasonal oscillation. Ph.D. Dissertation, Department of Meteorology, University of Reading, Reading, UK

Matthews AJ, Hoskins BJ, Slingo JM, Blackburn M (1996) Development of convection along the SPCZ within a Madden-Julian Oscillation. Q J Roy Meteorol Soc 122: 669-688

Murakami T, Nakazawa T (1984) On the 40-50 day oscillation during the 1979 Northern Hemisphere summer. Part I: phase propagation. J Meteorol Soc Japan 62:440-468.

Murakami T, Chen LX, Xie A, Shrestha ML (1986) Eastward propagation of 30-60 day perturbations as revealed from outgoing longwave radiation. J Atmos Sci 43:961-971

Neelin JD, Held IM, Cook KH (1987) Evaporation-wind feedback and low-frequency variability in the tropical atmosphere. J Atmos Sci 44: 2341-2348

Nishi N (1989) Observational study on the 30-60 day variations in the geopotential and temperature

fields in the equatorial region. J Meteorol Soc Japan 67: 187-203

Park C-K, Straus DM, Lau K-M (1990) An evaluation of the structure of the tropical intraseasonal oscillations in three general circulation models. J Meteorol Soc Japan 68 403-417

Phillips TJ (1994) A summary documentation of the AMIP models. PCMDI Report No. 18, Lawrence Livermore National Laboratory, 7000 East Ave, Livermore, CA 94550 USA; also via http://www-pcmdi.llnl.gov/phillips/modldoc/amip/amip.html

Pitcher EJ, Geisler JE (1987) The 40- to 50-day oscillation in a perpetual January simulation with a general circulation model. J Geophys Res 92: 11,971-11,978

Rosen RD, Salstein DA (1983) Variations in angular momentum on global and regional scales and the length of day. J Geophys Res 88: 5451-5470

Rui H, Wang B (1990) Development characteristics and dynamic structure of tropical intraseasonal convective anomalies. J Atmos Sci 47: 357-379

Salby ML, Garcia R, Hendon HH (1994) Planetary-scale circulations in the presence of climatological and wave-induced heating. J Atmos Sci 51: 2344-2367

Slingo JM, Madden RA (1991) Characteristics of the tropical intraseasonal oscillation in the NCAR community climate model. Q J Roy Meteorol Soc 117:1129-1169

Slingo JM, Sperber KR, Morcrette J-J, Potter GL (1992) Analysis of the temporal behavior of convection in the tropics of the European Centre for Medium-Range Weather Forecasts Model. J Geophys Res 98: 18,119-18,135

Slingo JM, Sperber KR, Boyle JS, Ceron J-P, Dix M, Dugas B, Ebisuzaki W, Fyfe J, Gregory D, Gueremy J-F, Hack J, Harzallah A, Inness P, Kitoh A, Lau WK-M, McAvaney B, Madden R, Matthews A, Palmer TN, Park C-K, Randall D, Renno N (1995) Intraseasonal oscillations in 15 atmospheric general circulation models: Results from an AMIP diagnostic subproject. WCRP-88, WMO/TD-No. 661, WMO, Geneva 86pp

Slingo JM, Sperber KR, Boyle JS, Ceron J-P, Dix M, Dugas B, Ebisuzaki W, Fyfe J, Gregory D, Gueremy J-F, Hack J, Harzallah A, Inness P, Kitoh A, Lau WK-M, McAvaney B, Madden R, Matthews A, Palmer TN, Park C-K, Randall D, Renno N (1996) Intraseasonal oscillations in 15 atmospheric general circulation models: Results from an AMIP diagnostic subproject. Clim Dynam 12: 325-357

Sud YC, Walker GK (1992) A review of recent research on improvement of physical parameterizations in the GLA GCM. in Physical Processes in Atmospheric Models, Sikka DR, Singh SS, Eds, Wiley Eastern Ltd, 422-479

Sud YC, Walker GK (1993) A rain evaporation and downdraft parameterization to complement a cumulus updraft scheme and its evaluation using GATE data. Mon Wea Rev 121: 3019-3039

Tokioka T, Yamazaki K, Kitoh A, Ose T (1988) The Equatorial 30-60 day oscillation and the Arakawa-Schubert penetrative cumulus parameterization. J Meteor Soc Japan 66: 883-900.

von Storch H, Bruns T, Fischer-Bruns I, Hasselmann K (1988) Principal oscillation pattern analysis of the 30- to 60-day oscillation in general circulation model equatorial troposphere. J Geophys Res 93:

11,022-11,036

Weickmann KM, Lussky GR, Kutzbach JE (1985) Intraseasonal (30-60 day) fluctuations of outgoing longwave radiation and 250mb streamfunction during northern winter. Mon Wea Rev 113: 941-961

Weickmann KM, Gutzler DS, Kiladis GN, Meehl GA, Wheeler M (1994) The eastward shift of convection and sea surface temperature during TOGA-COARE. Sixth Conference on Climate Variations. January 23-28, 1994, Nashville, TN, available from the American Meteorological Society, 45 Beacon St, Boston, MA 02108 USA

WMO (1995) Proceedings of the first international AMIP scientific conference. World Meteorological Organization/TD-No. 732, WCRP-92. held 15-19 May 1995, Monterey, CA, USA, 532pp

Yanai M, Esbensen S, Chu J-H (1973) Determination of bulk properties of tropical cloud clusters from large-scale heat and moisture budgets. J Atmos Sci 30: 611-627

Zhang C (1996a) Atmospheric intraseasonal variability at the surface in the tropical western Pacific Ocean. J Atmos Sci 53: 739-758

Zhang C (1996b) Coherence between SST and atmospheric variability in the western Pacific warm pool. Proceedings of the AMS Conference on the Global Ocean-Atmosphere-Land System (GOALS), Atlanta, Georgia, J112-J116

Zhang GJ, McPhaden MJ (1995) The relationship between sea surface temperature and latent heat flux in the equatorial Pacific. J Clim 8: 589-605

Return to Table of Contents

For more information about this report please contact Ken Sperber sperber@pcmdi.llnl.gov.
For technical feedback about this page, contact: Anna McCravy mccravy1@llnl.gov.

Last updated October 25, 1996.
Return to PCMDI home page.

 and LLNL Disclaimers
UCRL-ID-125333

Fig. 5. Time-longitude plot of 20-100 day bandpass filtered 200hPa 10°N-10°S averaged velocity potential for the period November-May 1987/88 from NCEP/NCAR reanalysis. Enhanced divergent outflow, corresponding to the active phase of the intraseasonal oscillation, is shaded. Contours are plotted at an interval of $2x10^6$ m^2 s^{-1}. Also shown is the pentad averaged intraseasonal oscillation (IO) index based on the average of the filtered velocity potential between 100°-140°E (the region between the vertical bars in the time-longitude plots). To show the strength of the IO during this period, the index has been standardized by removal of the mean and division by the standard deviation for 17 years of NCEP/NCAR reanalysis (1979-1995).

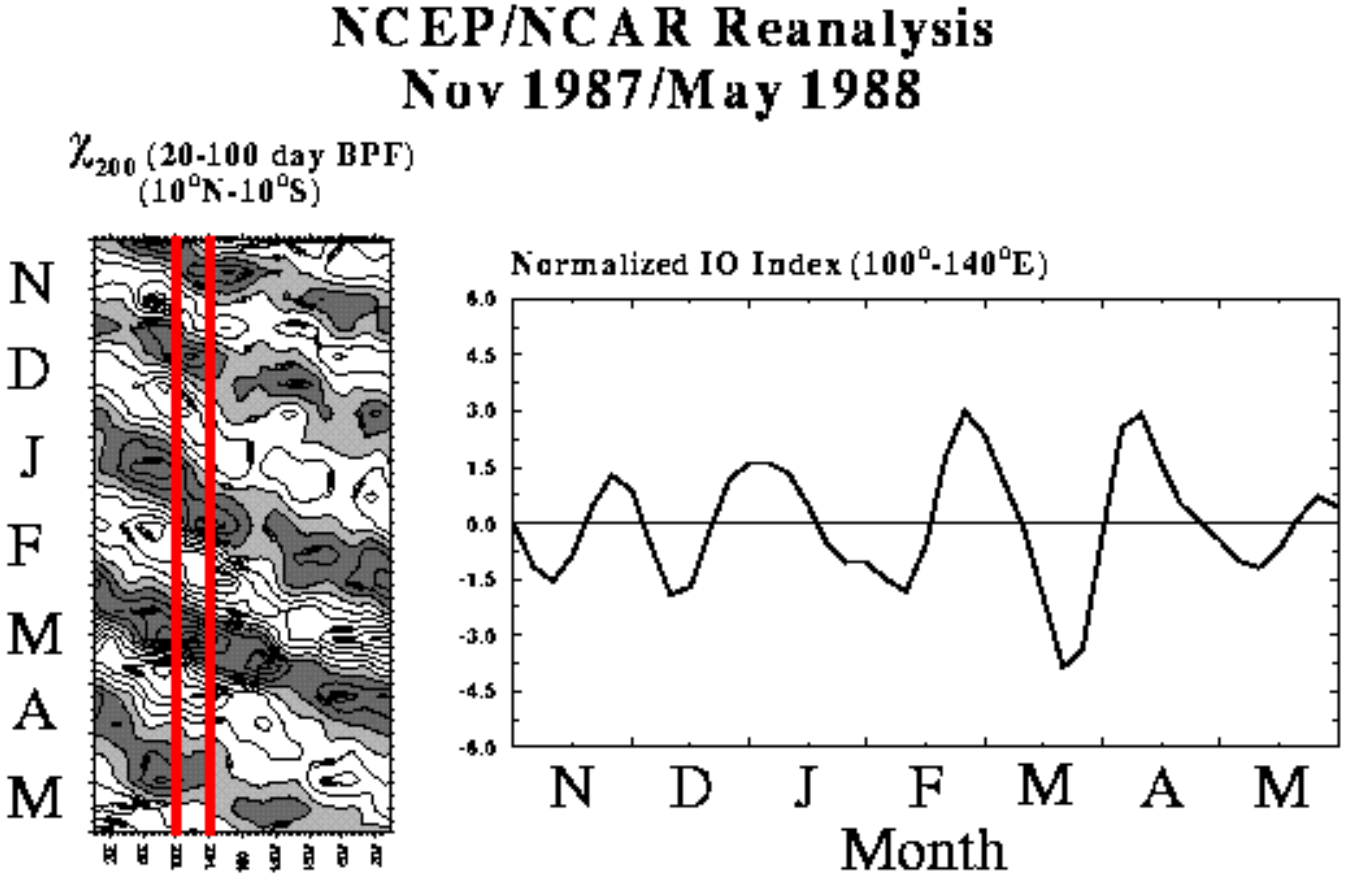

Fig. 1. Mean OLR for December/January/February/March (DJFM) 1979/80-1987/88. The observed OLR is from the NOAA satellite archive, and the simulated data are from the GLA and UKMO AMIP integrations.

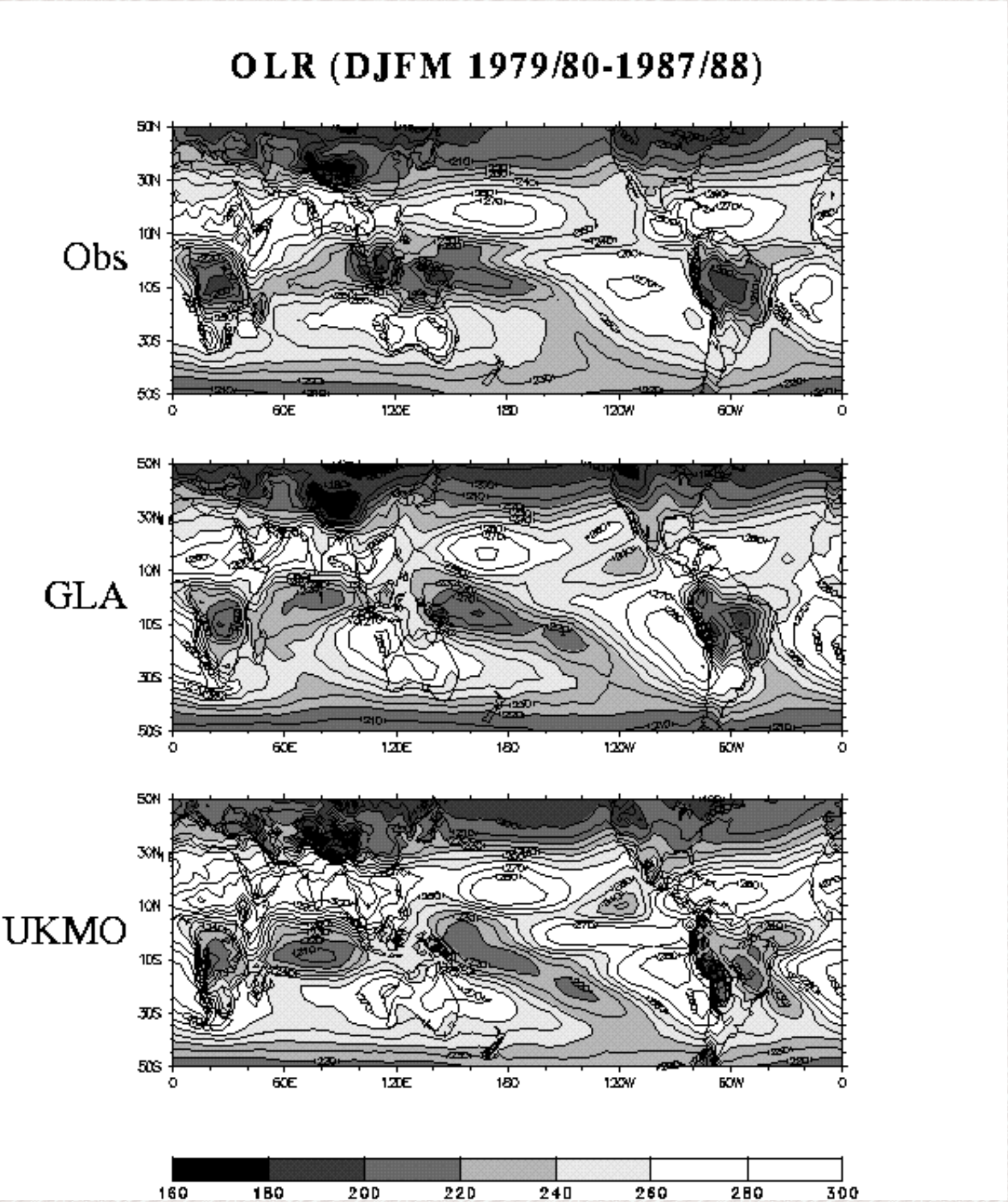

Fig. 2. Observed, GLA and UKMO standard deviations of OLR based on the average variance from all DJFM periods from 1979/80-1987/88. Also given is the percent of the OLR variance explained by periods of 30-70 days.

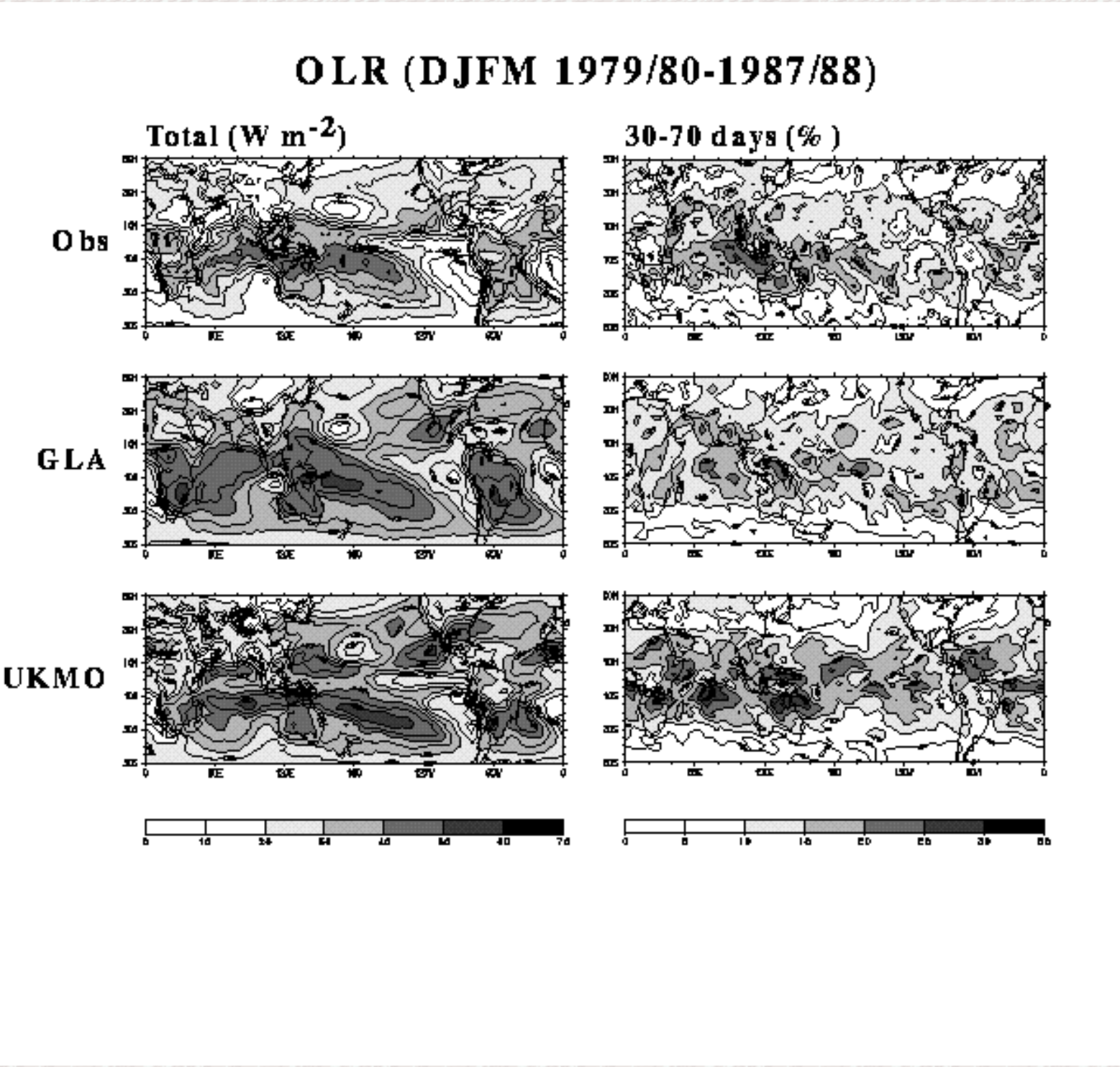

Fig. 3. First EOF of upper-level eddy-streamfunction (filtered to isolate intraseasonal time scales) for DJF 1982/83-1989/90. Data from ECMWF/JDP analyses (Matthews 1993) are compared with NCEP/NCAR reanalysis. The schematic diagram indicates the dynamical structure associated with the active phase (enhanced convection) of the intraseasonal oscillation. The dominant heating associated with the IO is located in the vicinity of the Maritime continent.

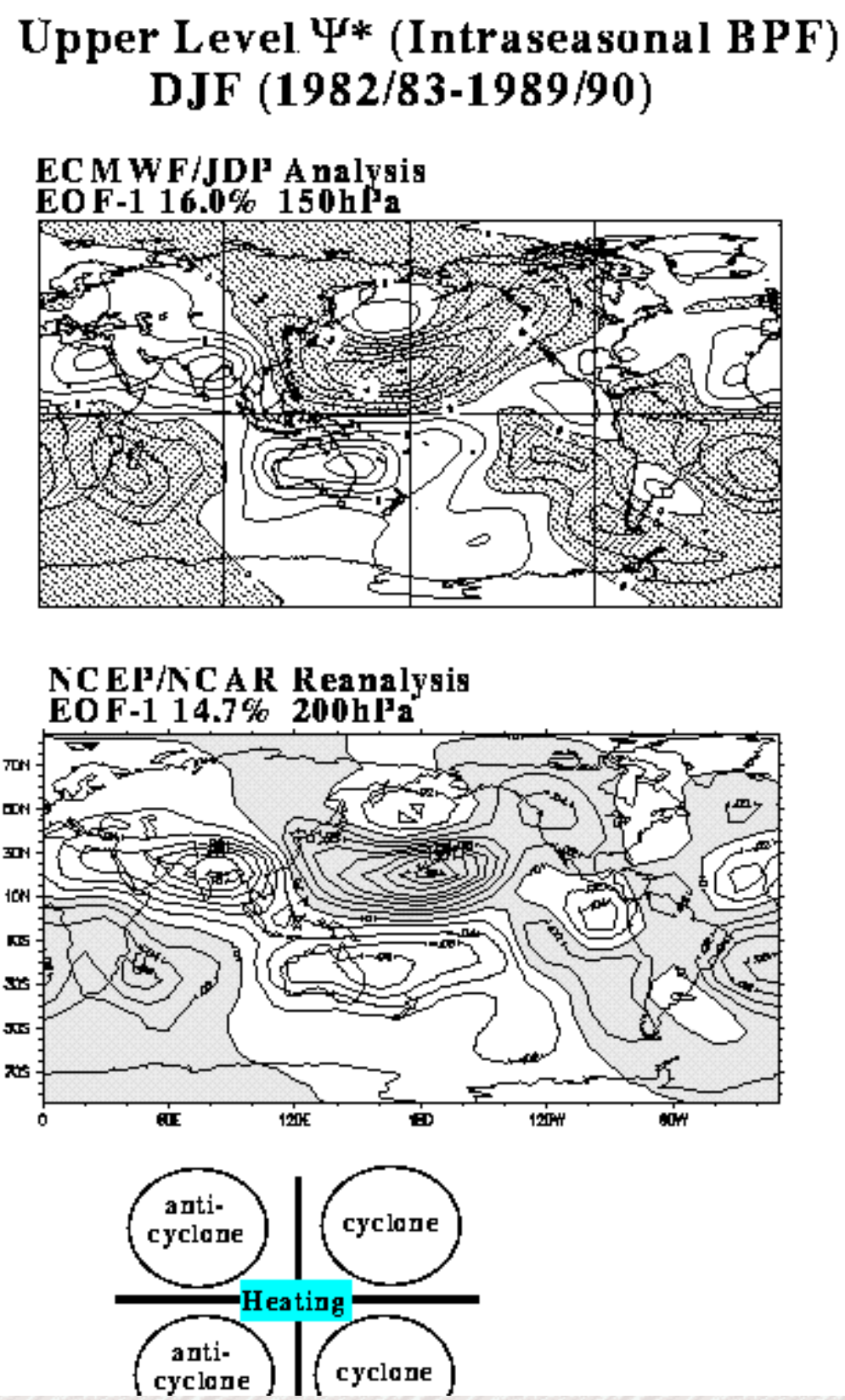

Fig. 4. First and second EOF's of 20-100 day bandpass filtered 200hPa eddy-streamfunction for November-May 1979/80-1987/88 from NCEP/NCAR reanalysis, and the GLA and UKMO AMIP integrations.

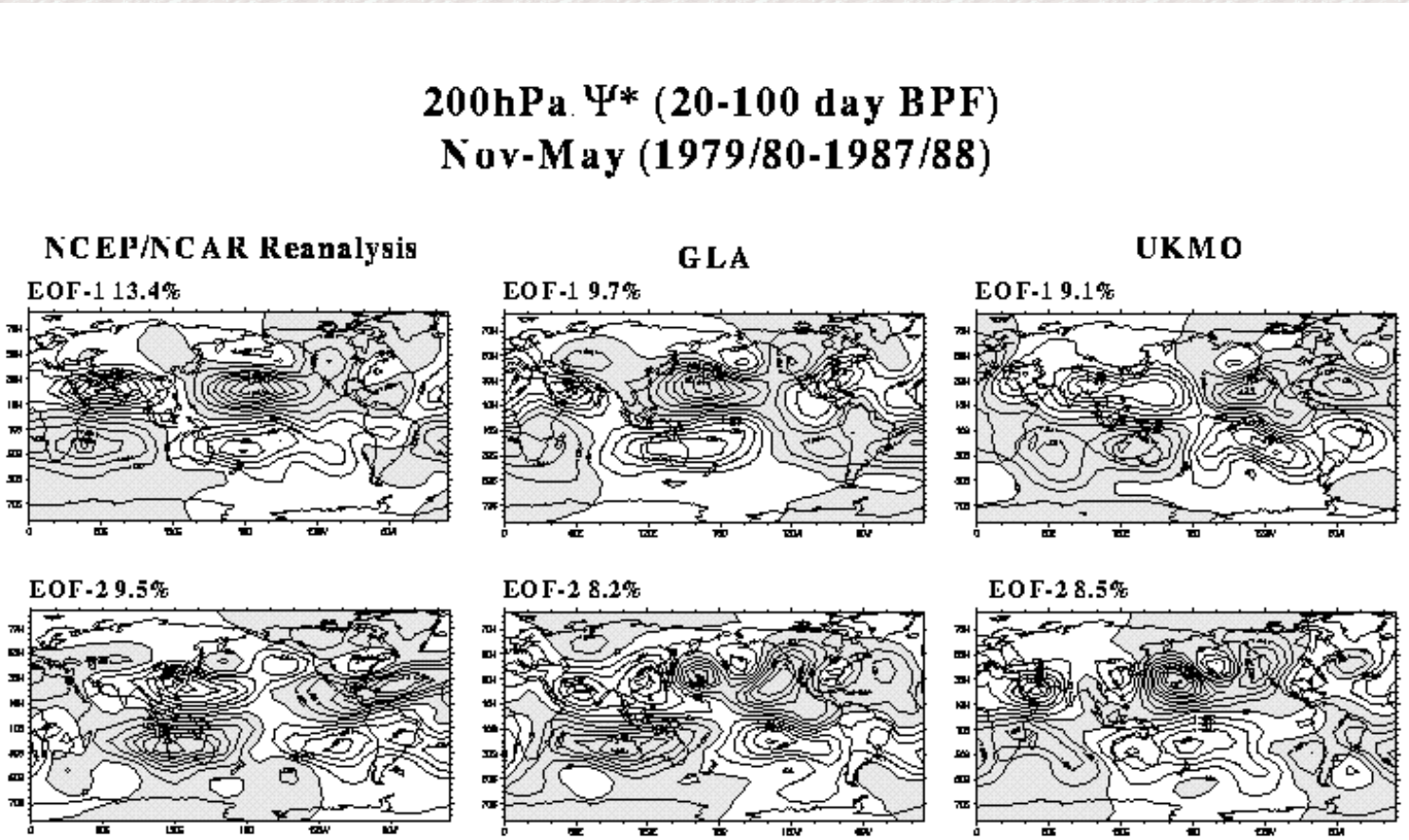

Fig. 6. Correlations of the pentad averaged NCEP/NCAR reanalysis IO index from Fig. 5 with observed (NOAA) satellite derived outgoing longwave radiation at various time lags. Positive (negative) correlations correspond to enhanced (suppressed) convection during the active phase of the IO. Positive (negative) correlations significant at ≥95% confidence level are shaded grey (black). The correlations are calculated from 43 pentads of data, and the 95% confidence level is |r|~0.3 based on 41 degrees of freedom. Since estimating the actual number of degrees of freedom is difficult, positive correlations are contoured from 0.3 at an increment of 0.1.

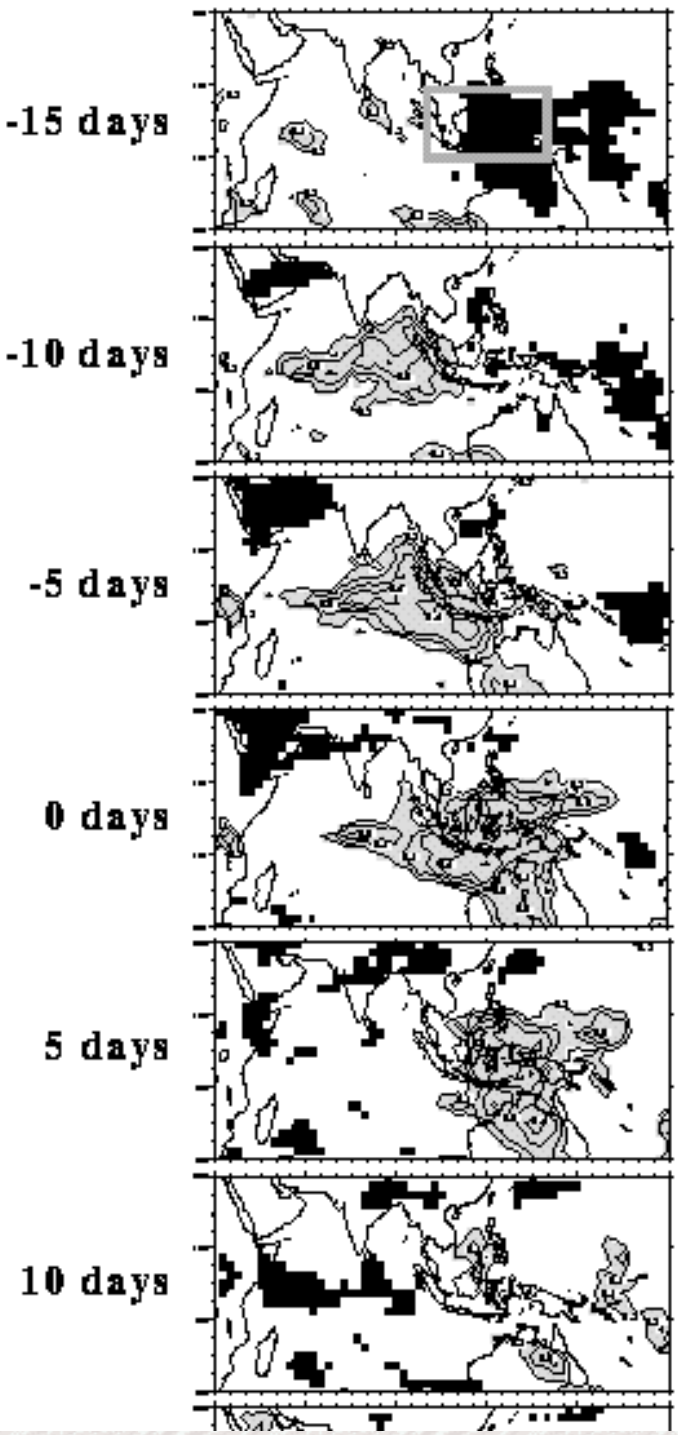

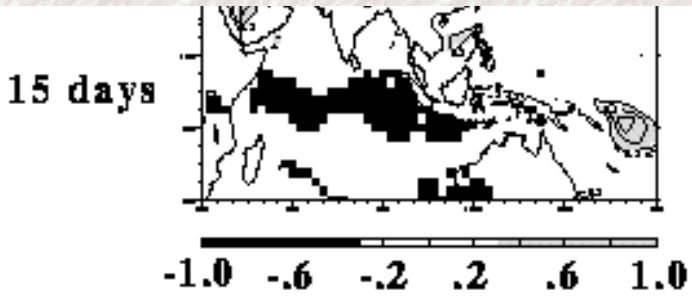
15 days
-1.0
-.6
-.2
.2
.6
1.0

Fig. 7. The time lag at which a significant positive correlation between the IO index and the OLR is a maximum is plotted. Lags from -15 days to +15 days are considered. For the NCEP/NCAR reanalysis case study, the results are based on significant positive (grey) correlations in Fig. 6. The maximum positive correlations are contoured beginning from 0.3 at an increment of 0.1. Also shown are the time-longitude plots of 20-100 day bandpass filtered 200hPa 10°N-10°S averaged velocity potential for the period November-May and the simulated IO index/OLR correlation time lag plots for the case study periods from the GLA and UKMO simulations. The vertical red lines indicate the region from which each IO index is obtained (100°-140°E).

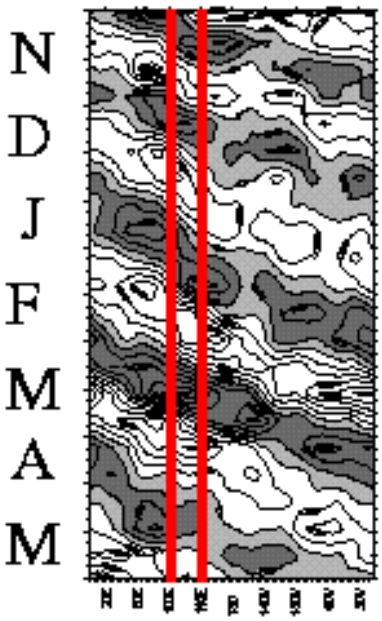

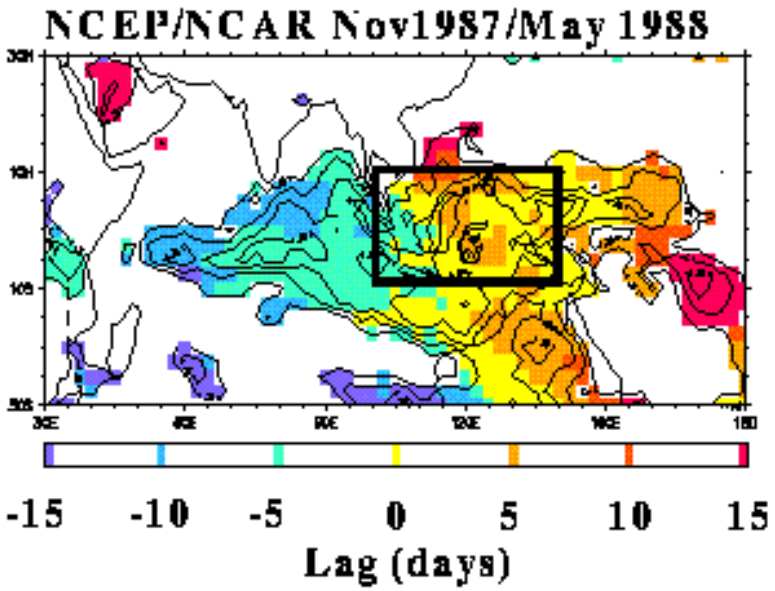

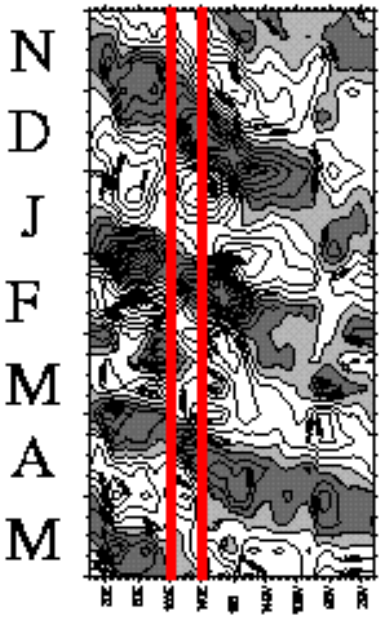

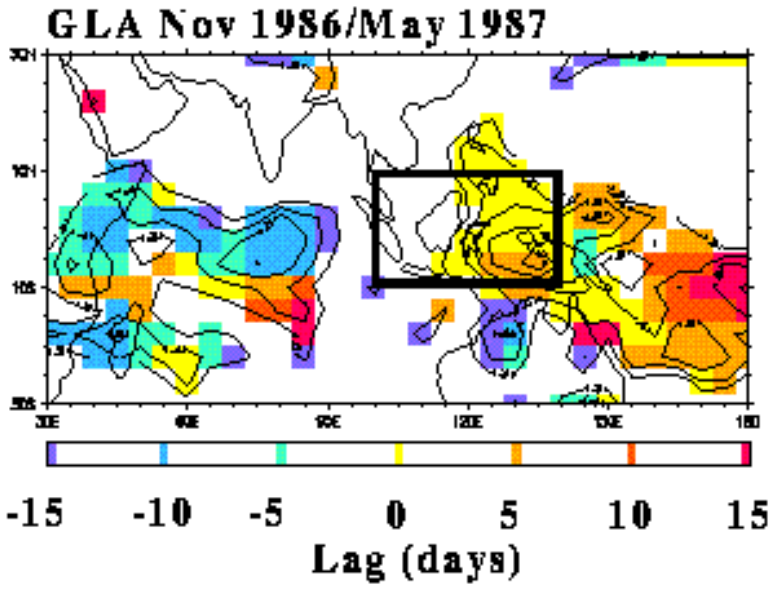

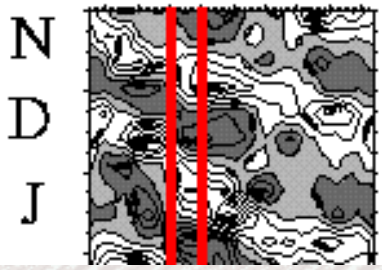

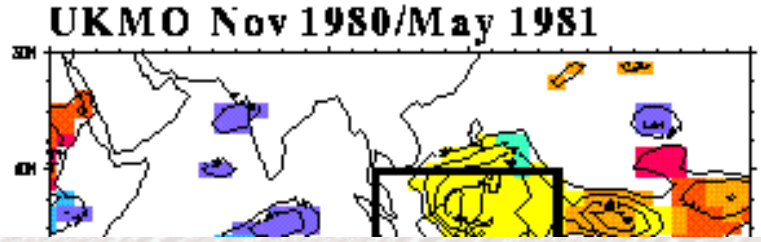

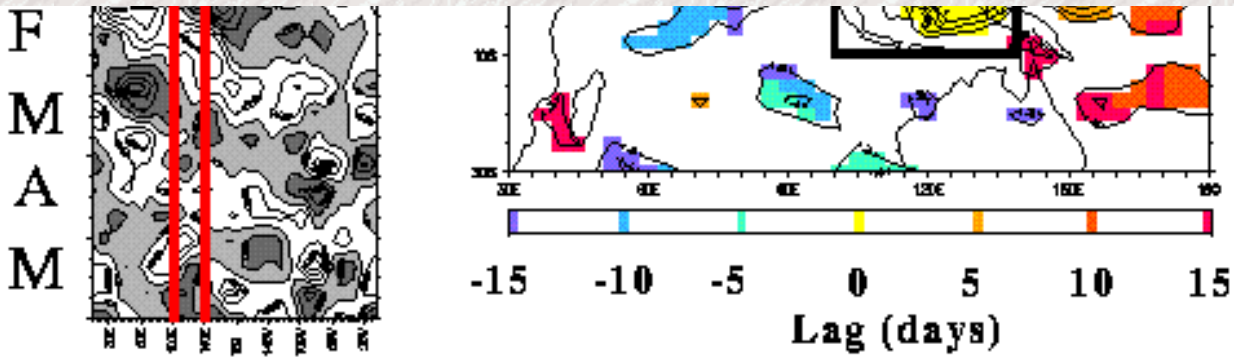
F
M
A
M
-15
-10
-5
0
5
10
15
Lag (days)

Fig. 8. First and second EOF's and principal components of 20-100 day bandpass filtered 200hPa and 850hPa eddy-streamfunction for November-May 1987/88 from NCEP/NCAR reanalysis. Also plotted is the (non-standardized) IO index time series used for the OLR correlation in Figs. 6 and 7.

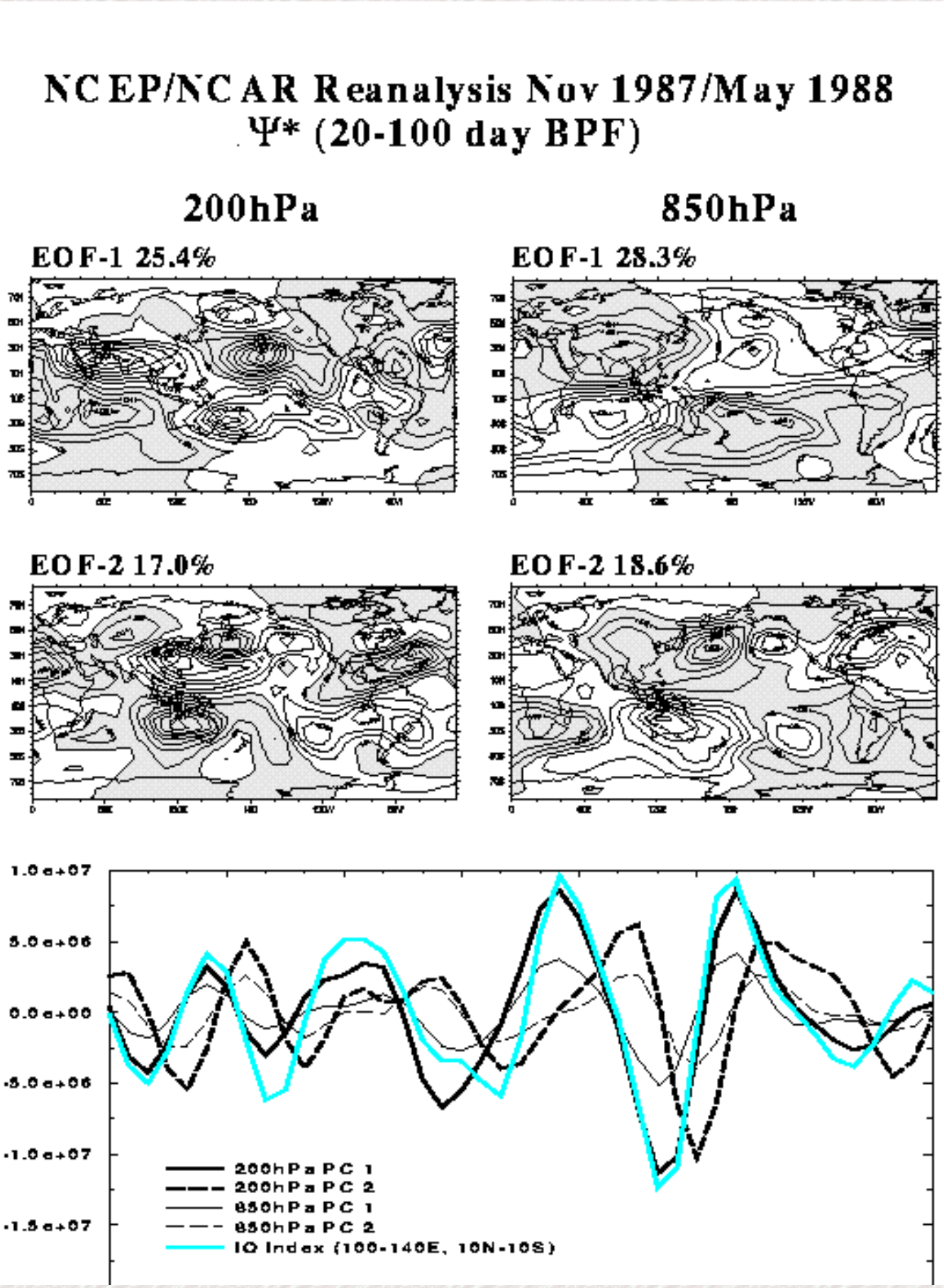

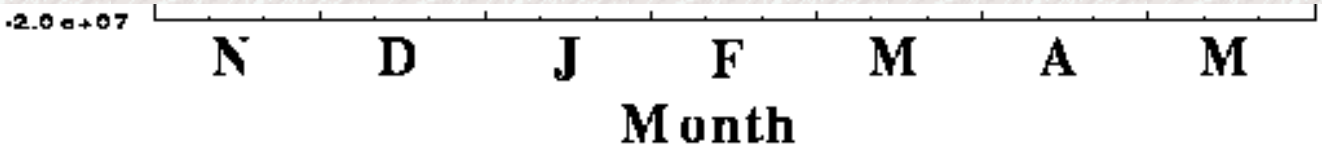
2.0e+07
N
D
J
F
M
A
M
Month

Fig. 10. As Fig. 8, but from the 1980/81 UKMO case study.

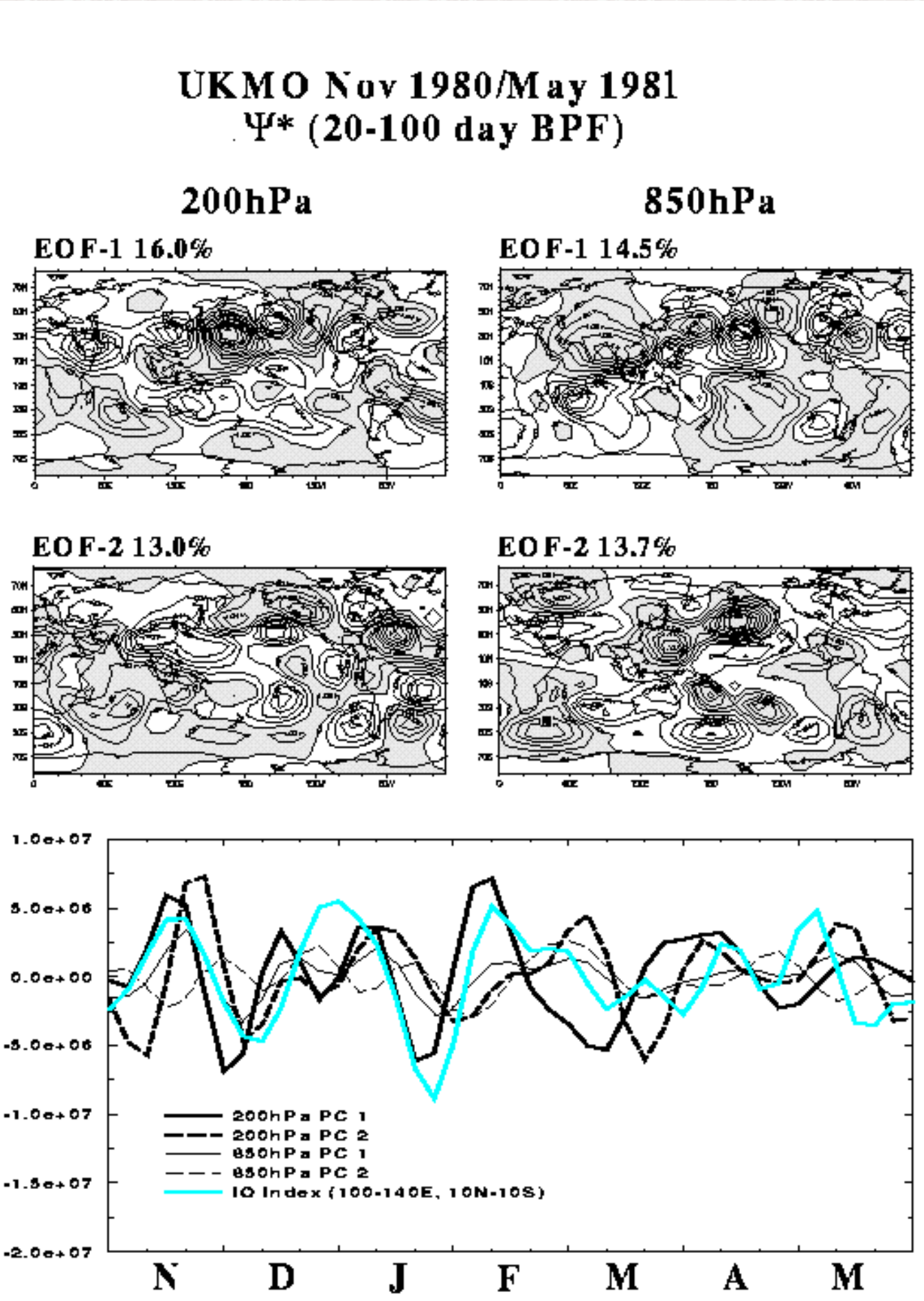

Month

Fig. 9. As Fig. 8, but from the 1986/87 GLA case study. An additional IO index for the region 60°-100°E, 10°N-10°S is plotted.

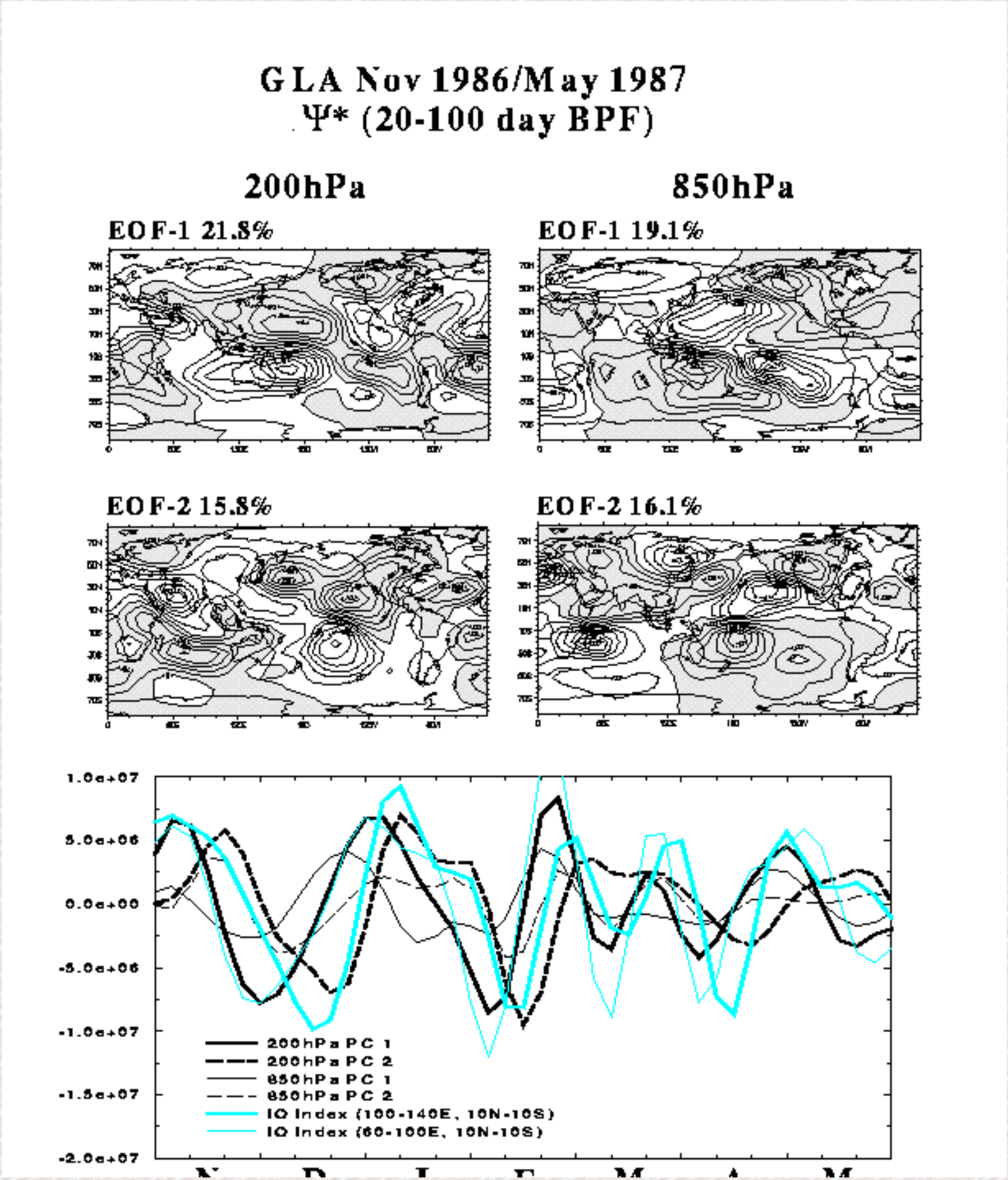

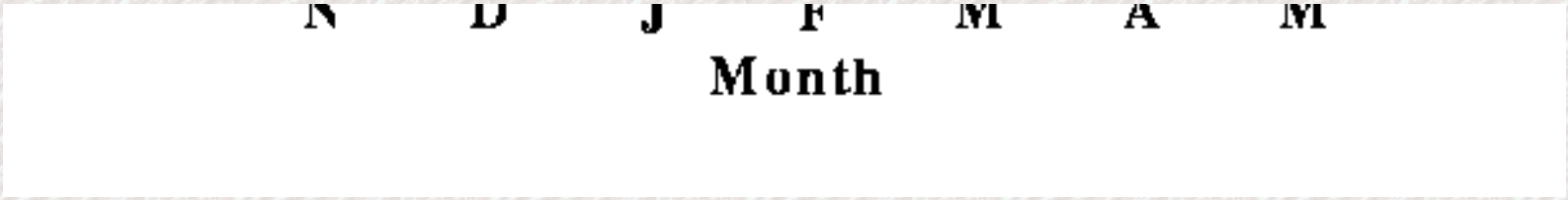
N
D
J
F
M
A
M
Month

Fig. 11. Time lags at which a significant positive (negative) correlation between the IO index and 200hPa and 850hPa 20-100 day bandpass filtered eddy-streamfunction is a maximum (minimum) are plotted. Positive and negative correlations provide information about the eastward propagation of cyclones and anticyclones during the active phase of the IO. The propagation of the cyclonic anomalies is based on positive (negative) correlation between the IO index and eddy-streamfunction in the Northern (Southern) Hemisphere. The propagation of the anticyclonic anomalies is based on negative (positive) correlation between the IO index and eddy-streamfunction in the Northern (Southern) Hemisphere. Also shown are schematic diagrams of the anomalous flow relative to the location of the enhanced convection at time-lag 0 based on data in Fig.7. Data are presented for the NCEP/NCAR reanalysis 1987/88 case study, the GLA 1986/87 case study and the UKMO 1980/81 case study.

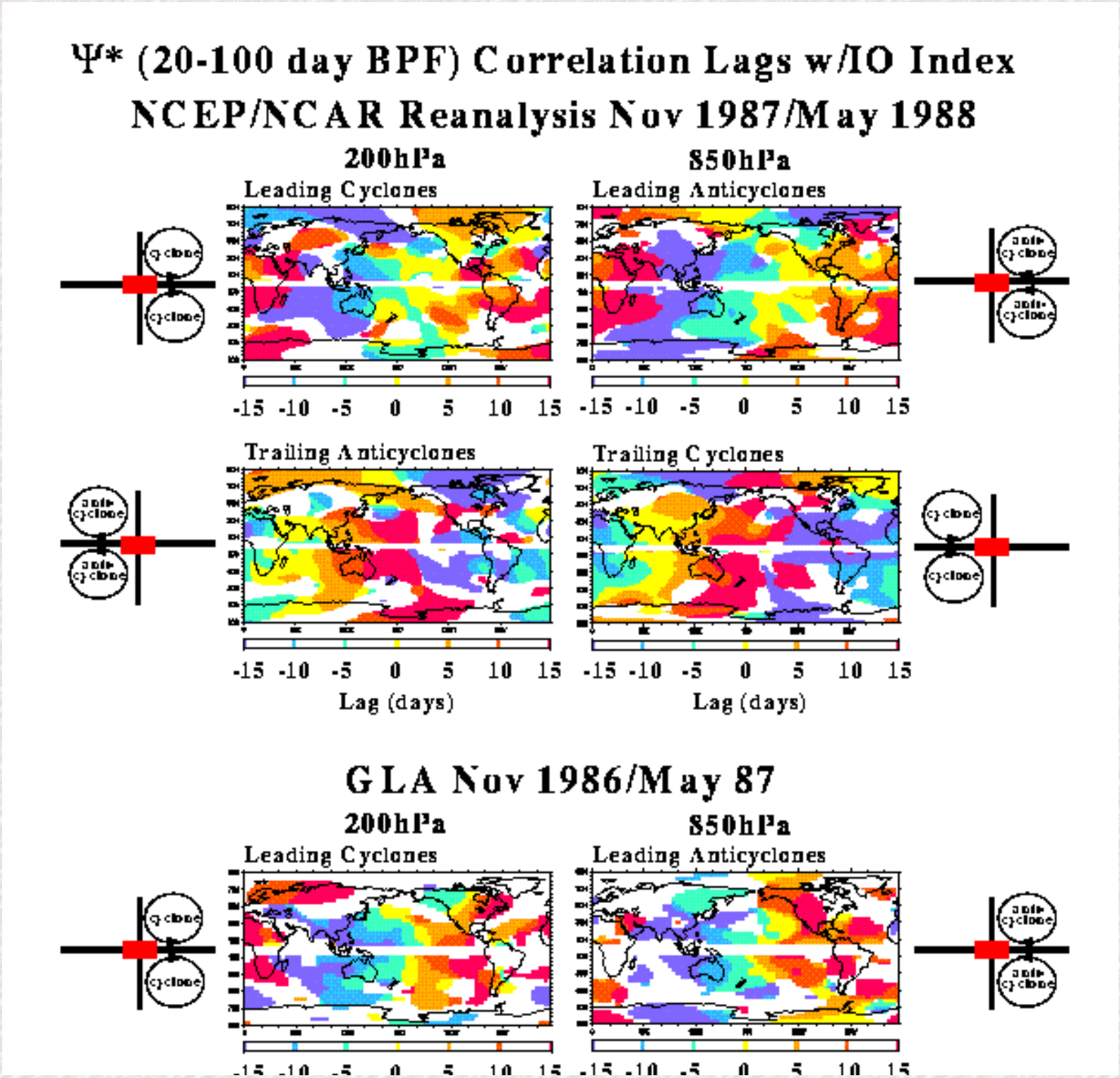

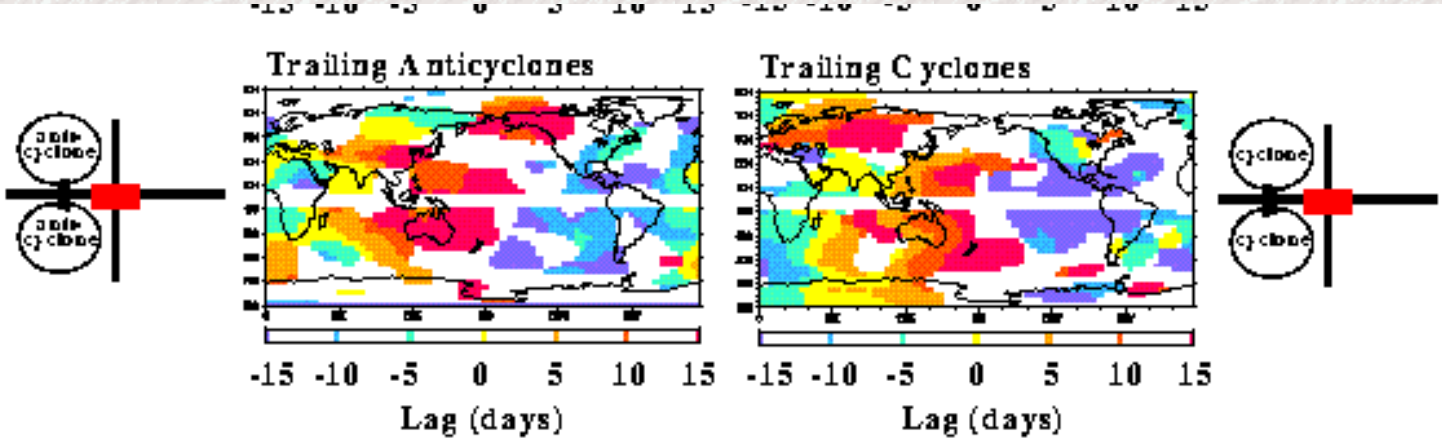

UKMO Nov 1980/May 81

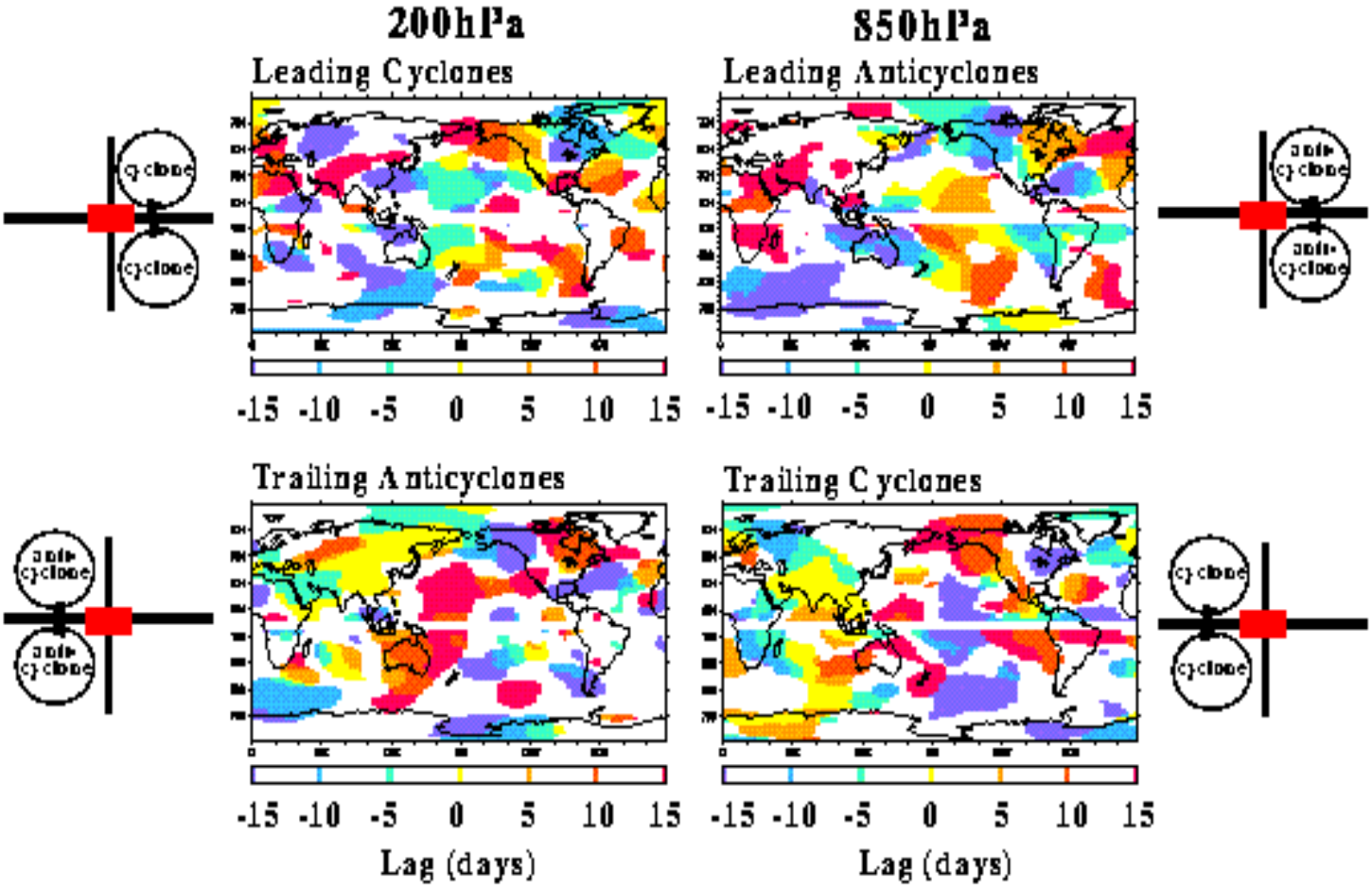

Fig. 12. Total OLR and 20-100 day bandpass filtered divergence in a frame of reference relative to the eastward propagation of the active phase of the intraseasonal oscillation over the western Pacific Ocean (105°-180°E). OLR $\leq$210w m^{-2} is contoured at an interval of -10w m^{-2}. Divergence and convergence (negative divergence) are shaded at an interval of 2 x 10^{-6} s^{-1} at 200hPa and the surface. At 850hPa, the shading is at an interval of 1 x 10^{-6} s^{-1}.

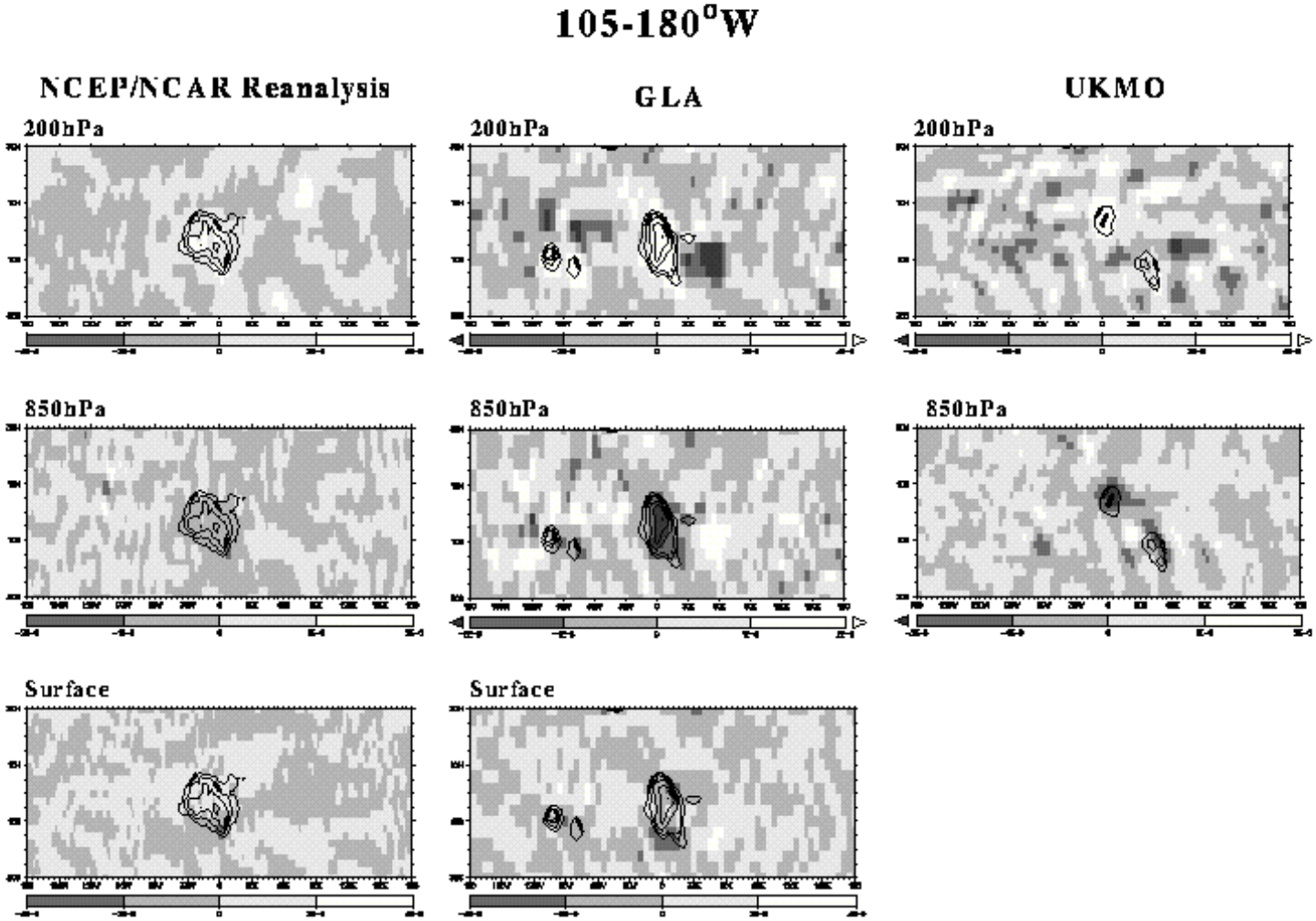

Fig. 13. Total OLR, latent heat flux, and surface winds (850hPa for UKMO since surface winds were not available) in a frame of reference relative to the eastward propagation of the active phase of the intraseasonal oscillation over the western Pacific Ocean (105°-180°E). OLR $\leq$210w m^{-2} is contoured at an interval of -10w m^{-2}. The latent heat flux (w m^{-2}) is shaded, with the strongest evaporation shaded white. A vector of unit length equals 4m s^{-1}.

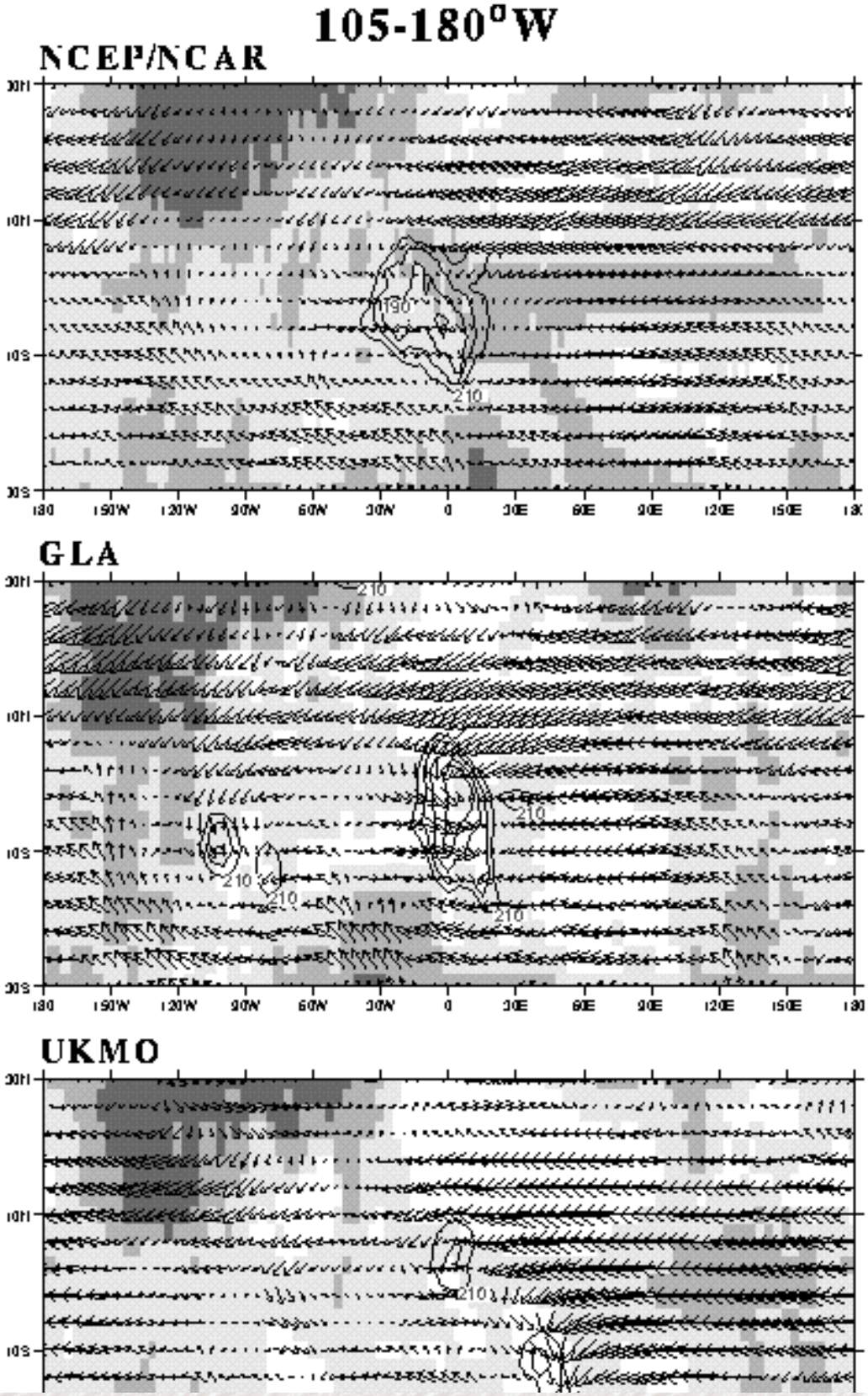

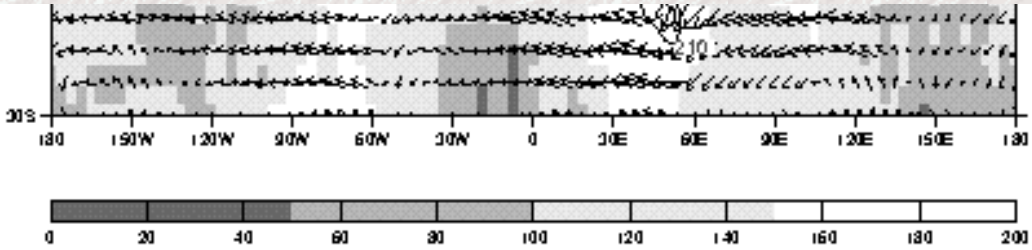
20S
180
150W
120W
90W
60W
30W
0
30E
60E
90E
120E
150E
180
0
20
40
60
80
100
120
140
160
180
200

Fig. 14. Correlations of the pentad averaged IO indexes from the reanalysis and the model simulations with 20-100 day bandpass filtered latent heat flux. Negative (positive) correlations correspond to enhanced (suppressed) evaporation during the active phase of the IO. Negative (positive) correlations significant at ≥95% confidence level are shaded grey (black). Negative correlations are contoured from -0.3 at an increment of -0.1.

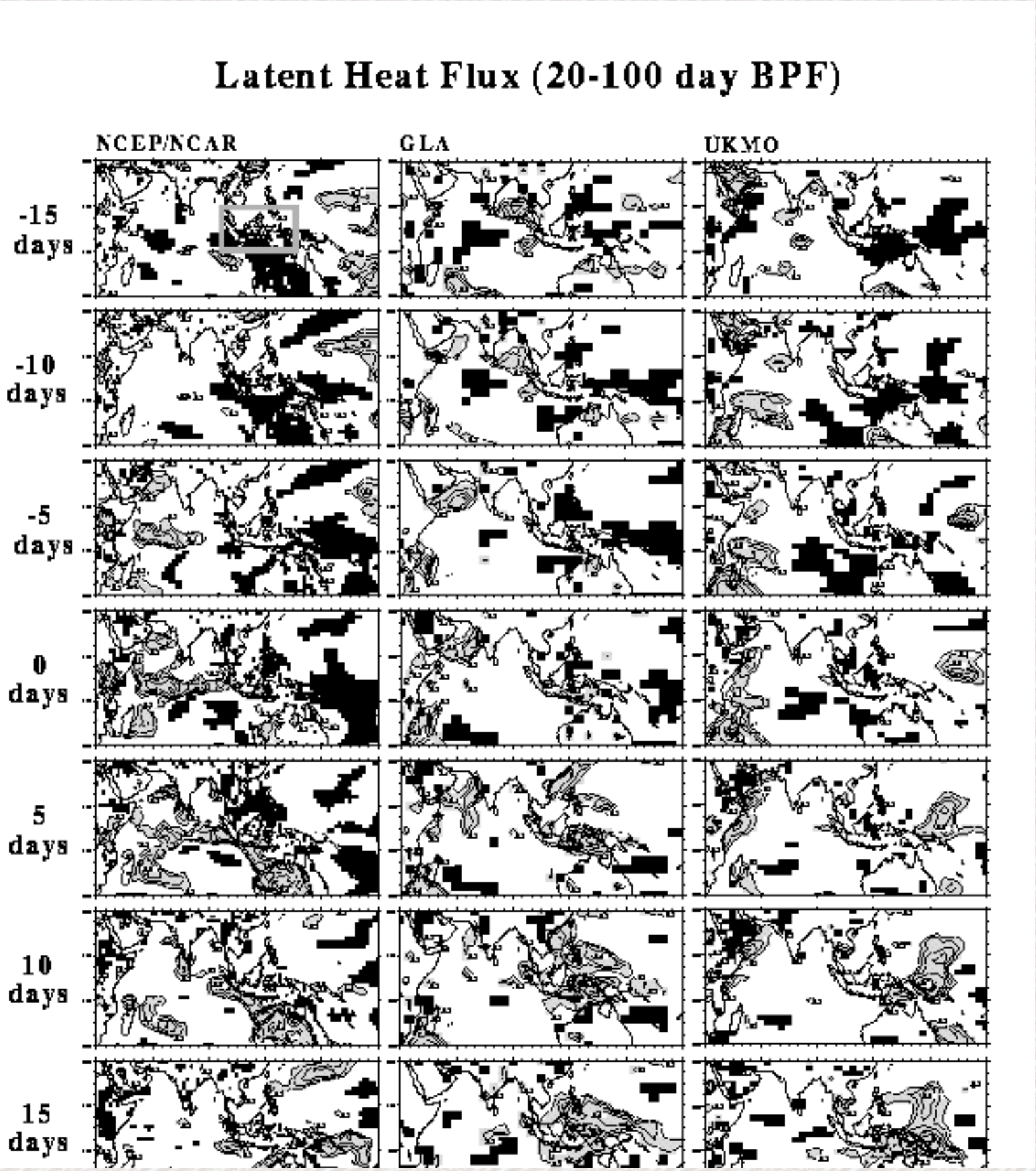

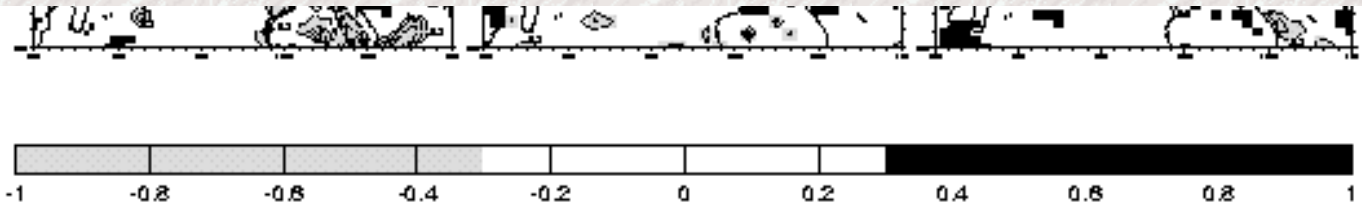
-1
-0.8
-0.6
-0.4
-0.2
0
0.2
0.4
0.6
0.8
1

Fig. 15. Correlations of the pentad averaged reanalysis IO index with 20-100 day bandpass filtered sea surface temperature, and surface skin temperature from the ECMWF reanalysis at various time lags. Correlations significant at ≥95% confidence level are plotted as gridpoint data. Negative correlations (shaded yellow-red) correspond to warm SST anomalies, positive correlations (shaded blue-purple) correspond to cold SST anomalies during the active phase of the IO. Isolines of the correlation of the IO index with unfiltered OLR are also shown (as in Fig. 6). Positive (negative) correlations indicate enhanced (suppressed) convection are plotted as blue (red) isolines. Correlations significant at ≥95% are contoured (|r|≥0.3; at an increment of |0.1|).

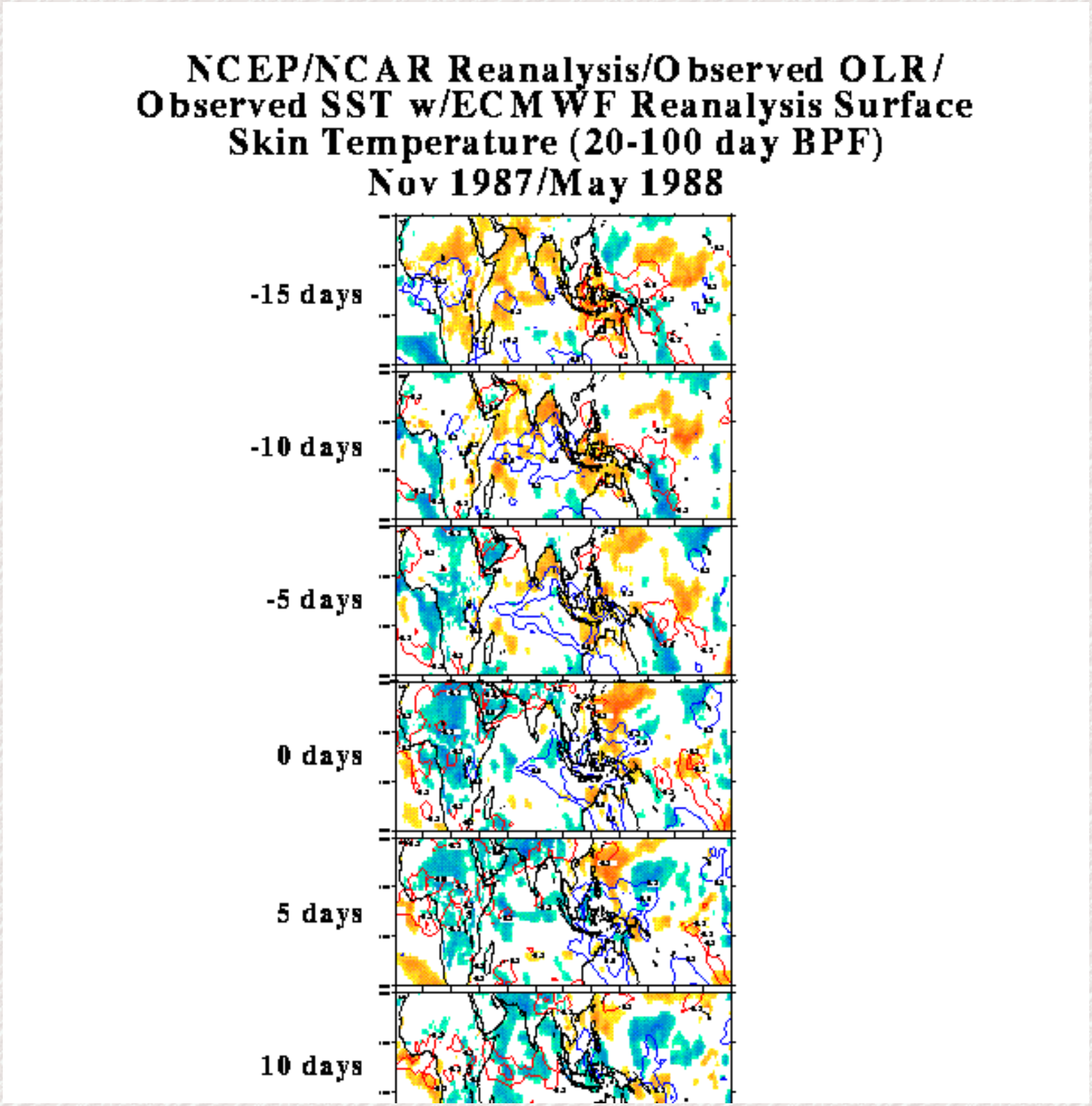

15 days